ABSTRACT

EXPLORING TOPOLOGICAL PHONONS IN DIFFERENT LENGTH SCALES: MICROTUBULES AND ACOUSTIC METAMATERIALS

by
Ssu-Ying Chen

The topological concepts of electronic states have been extended to phononic systems, leading to the prediction of topological phonons in a variety of materials. These phonons play a crucial role in determining material properties such as thermal conductivity, thermoelectricity, superconductivity, and specific heat. The objective of this dissertation is to investigate the role of topological phonons at different length scales.

Firstly, the acoustic resonator properties of tubulin proteins, which form microtubules, will be explored The microtubule has been proposed as an analog of a topological phononic insulator due to its unique properties. One key characteristic of topological materials is the existence of edge modes within the energy gap. These edge modes allow energy to be transferred at specific frequencies along the edges of the material, while the bulk remains unaffected. In the case of microtubules, its ability to store vibrational energy at its edges and the sensitivity to changes in local bulk structure align with the properties of topological insulators. Furthermore, the appearance of edge modes in topological phononic insulators is determined by the local interactions of the bulk material. Even small changes in the local structure can shift the resonant frequency of the edge mode or completely extinguish it. Similarly, the ability of microtubules to shorten or overcome energy barriers is greatly affected by changes in their local bulk structure. This suggests a parallel between the impact of local bulk structure on both topological insulators and microtubules. This similarity has led to the proposal that microtubules could serve as an analog of topological phononic insulators, providing insights into their dynamics and potential applications in fields such as chemotherapy drug development and nanoscale materials.

Secondly, the application of topological phonons in the realm of acoustic metamaterials will be examined. Acoustic waves have recently become a versatile platform for exploring and studying various topological phases, showcasing their universality and diverse manifestations. The unique properties of topological insulators and their surface states heavily rely on the dimension and symmetries of the material, making it possible to classify them using a periodic table of topological insulators. However, certain combinations of dimensions and symmetries can impede the achievement of topological insulation. It is of utmost importance to preserve symmetries in order to maintain the desired topological properties, which necessitates careful consideration of coupling methods. In the context of discrete acoustic resonant models, efficiently coupling resonators while simultaneously preserving symmetry poses a challenging question. In this part, a clever experimental approach is proposed and discussed to couple acoustic crystals. This modular platform not only supports the existence of topologically protected edge and interface states but also offers a convenient setup that can be easily assembled and disassembled. Furthermore, inspired by recent theoretical advancements that draw on techniques from the field of C^*-algebras for identifying topological metals, the present study provides direct observations of topological phenomena in gapless acoustic crystals. Through these observations, a general experimental technique is realized and developed to demonstrate the topology of such systems. By employing the method of coupling acoustic crystals, the investigation unveils robust boundary-localized states in a topological acoustic metal and presents a reinterpretation of a composite operator as a new Hamiltonian. This reinterpretation enables the direct observation of a topological spectral flow and facilitates the measurement of topological invariants.

Through these investigations, the aim of this dissertation is to deepen our understanding of the significance and potential applications of topological phonons in diverse systems.

EXPLORING TOPOLOGICAL PHONONS IN DIFFERENT LENGTH SCALES: MICROTUBULES AND ACOUSTIC METAMATERIALS

by
Ssu-Ying Chen

A Dissertation
Submitted to the Faculty of
New Jersey Institute of Technology
in Partial Fulfillment of the Requirements for the Degree of
Doctor of Philosophy in Applied Physics

Department of Physics

August 2023

APPROVAL PAGE

EXPLORING TOPOLOGICAL PHONONS IN DIFFERENT LENGTH SCALES: MICROTUBULES AND ACOUSTIC METAMATERIALS

Ssu-Ying Chen

Dr. Camelia Prodan, Dissertation Advisor — Date
Associate Professor of Physics, NJIT

Dr. Keun Hyuk Ahn, Committee Member — Date
Associate Professor of Physics, NJIT

Dr. Benjamin P. Thomas, Committee Member — Date
Associate Professor of Physics, NJIT

Dr. Sagnik Basuray, Committee Member — Date
Associate Professor of Chemical and Materials Engineering, NJIT

Dr. Edward Bonder, Committee Member — Date
Professor of Biological Sciences, Rutgers University, Newark

BIOGRAPHICAL SKETCH

Author: Ssu-Ying Chen

Degree: Doctor of Philosophy

Date: August 2023

Undergraduate and Graduate Education:

- Doctor of Philosophy in Applied Physics,
  New Jersey Institute of Technology, Newark, NJ, 2023
- Bachelor of Physics,
  National Taiwan Normal University, Taiwan, 2017

Major: Applied Physics

Publications:

Cheng, W., Cerjan, A., Chen, SY., Prodan, E., Loring, T., & Prodan, C. (2023). Revealing topology in metals using experimental protocols inspired by K-theory. *Nature Communications 14*(1), 3071.

Chen, SY., & Prodan, C. (2023). Symmetry-preserving coupling method for topological acoustic metamaterials. *arXiv:2303.06065.*

Chen, SY., Aslam, A., Apigo, D., Basuray, S., & Prodan, C. (2020). Isolating a single microtubule in nanofluidic device. *arXiv:2302.08433.*

Presentations:

Chen, SY. (2023, March 5-10). Simple coupling method for topological acoustic metamaterial measurement. *Oral presentation*. American Physical Society March Meeting, Las Vegas, NV, United States.

Cheng, SY. (2019, March 4-8). Topological phonons in microtubules: The link between local structure and dynamics of microtubules. *Oral presentation*. American Physical Society March Meeting, Boston, MA, United States.

Cheng, SY. (2018, February 17-21). Topological phonons in microtubules: The link between local structure and dynamics of microtubules. *Poster presentation*. Biophysical Society Annual Meeting, San Francisco, CA, United States.

Cheng, SY. (2017, June 17-20). The Correlation between bacterial transcription and translation at single molecule level in living cells. *Poster presentation*. Biophysical Society June Meeting, Taipei, Taiwan.

I dedicate this dissertation to my beloved family, whose unwavering support has been the cornerstone of my academic journey.

ACKNOWLEDGMENT

I would like to express my deepest appreciation to Dr. Camelia Prodan for her invaluable support throughout my PhD journey. First and foremost, I am truly honored to have had the privilege of being her PhD student. Dr. Prodan has consistently provided unwavering guidance and encouragement, instilling in me a sense of professionalism and resilience even during challenging times. From the very beginning of my work on the microtubule project, she has been incredibly supportive and patient, consistently pushing me to strive for excellence. Her keen insights and constructive feedback have significantly enhanced my understanding of each research problem, as she has continuously pointed out areas of improvement and helped me refine my work. The trust and support she has shown throughout this endeavor have been truly transformative, and I am grateful for the knowledge and experience I have gained under her guidance. Once again, I extend my genuine thanks to Dr. Camelia Prodan for her mentorship, guidance, and belief in my abilities.

I extend my sincere appreciation to the members of my committee, Dr. Keun Hyuk Ahn, Dr. Sagnik Basuray, Dr. Benjamin Thomas, and Dr. Edward Bonder, for their valuable time spent attending my proposal defense and final defense. Their insightful comments and thought-provoking questions have inspired me to broaden my research from various perspectives.

I would like to express my gratitude to the W. M. Keck Foundation and the National Science Foundation grant DMR-1823800 for their financial support of my research and Research Assistant position. Additionally, I am grateful to the Department of Physics for its financial support of my research and Teaching Assistant position.

I also want to thank Dr. Emil Prodan, Dr. Massimo Ruzzene, and Dr. Chia-Fu Chou, who provided me the opportunities to engage in collaborative work. Their vast knowledge has greatly enriched my academic journey.

I would also like to acknowledge Dr. Yi-Ren Chang and Dr. Wen-Chin Lin for their genuine support and encouragement throughout my academic journey. It is thanks to their guidance and belief in my potential that I have been motivated to pursue further studies abroad and eventually embark on the path towards obtaining a PhD.

I am immensely grateful for the presence of wonderful friends during my time at the New Jersey Institute of Technology, and among them, I want to express my heartfelt thankfulness to Dr. Wenting Cheng. Her encouragement, friendship, and expertise in topological acoustic metamaterials have been invaluable to my academic journey. With her guidance, I have gained a deep understanding of this specialized field, which has been instrumental in reaching this stage of graduation. Special thanks go to my colleague and one of my closest friends, Dr. Arooj A. Aslam, for her steadfast guidance and assistance throughout my early PhD journey. Her expertise and mentorship in the microtubule project, as well as her company in cleanroom micro/nanofabrication, have been indispensable in expanding my knowledge and skills. The meaningful friendship we share has also brightened my days and provided me with a sense of warmth and firm support.

In addition, I would like to thank my loving, encouraging, and ever-supportive boyfriend, Kerwyn Daniel. Throughout my entire PhD journey, his understanding, patience, and endless support have provided me with a solid foundation and a sense of comfort during the ups and downs of this demanding academic pursuit. I am truly grateful for his faithful companionship, which has made this challenging journey all the more meaningful and rewarding.

Last but certainly not least, I would like to express my deepest gratitude to my beloved family. My esteemed father, Dr. Jun-Chu Chen, my cherished mother, Yen-Chu Hsu, my dear brother and sister, Pin-Zhu Chen, and Dr. Hui-Ju Chen. Their unwavering love, unconditional support, and solid belief in me have been the driving force behind my academic journey, and have shaped me into the person I am today. From the earliest stages of my life, they have nurtured me with care and provided me with the tools and opportunities to

pursue my dreams. Their continuous encouragement and guidance have instilled in me the resilience and determination to overcome challenges and strive for excellence. I recognize that without their love and support, none of the accomplishments achieved thus far would have been possible, and I am forever grateful for their presence in my life.

TABLE OF CONTENTS

TABLE OF CONTENTS
(Continued)

Chapter **Page**

LIST OF FIGURES

Figure **Page**

LIST OF FIGURES
(Continued)

Figure **Page**

LIST OF FIGURES
(Continued)

Figure **Page**

LIST OF FIGURES
(Continued)

Figure **Page**

Figure **Page**

LIST OF FIGURES
(Continued)

Figure **Page**

LIST OF FIGURES
(Continued)

Figure **Page**

CHAPTER 1

INTRODUCTION

1.1 Topological Phonons

The concepts of topology that originated in the study of electronic states have been extended to the realm of phonons, leading to the prediction of topological phonons in diverse materials. Phonons play a crucial role in determining various material properties, such as thermal conductivity, thermoelectricity, superconductivity, and specific heat. In topological phononics study, the focus is on exploring the unique behavior of phonons in materials with non-trivial topological features. [Yang et al., 2015]

Topology, in this context, refers to the geometric and connectivity properties of a material rather than its specific shape or size. Topological materials exhibit properties that are robust against certain perturbations and are protected by underlying symmetries. These materials possess a distinct energy band structure with band gaps and topologically protected edge or surface states. The presence of these protected states ensures that the material's properties remain stable even in the presence of defects or imperfections.

In the case of topological phonons, researchers investigate the behavior of phonons in materials. This includes studying the dispersion relations, group velocities, and mode profiles of phonons in these materials. The unique topological features of the material can give rise to exotic wave phenomena, such as the existence of protected phonon modes localized at the edges or surfaces of the material.

The study of topological phonons has both fundamental and practical implications. From a fundamental perspective, it allows for the exploration of novel wave phenomena and the understanding of how topology influences wave propagation in materials. On the practical side, topological phononics holds promise for developing new types of materials

with desired acoustic properties, such as the ability to control sound wave propagation or enhance sound insulation.

This dissertation aims to investigate the role of topological phonons across different length scales. Firstly, we will examine the acoustic resonator properties of tubulin proteins, which form microtubules, and explore their potential as phononic analog of topological insulators. Secondly, we will explore the application of topological phonons in the context of acoustic metamaterials. By studying these two aspects, we attempt to gain a deeper understanding of the significance and potential of topological phonons in diverse systems.

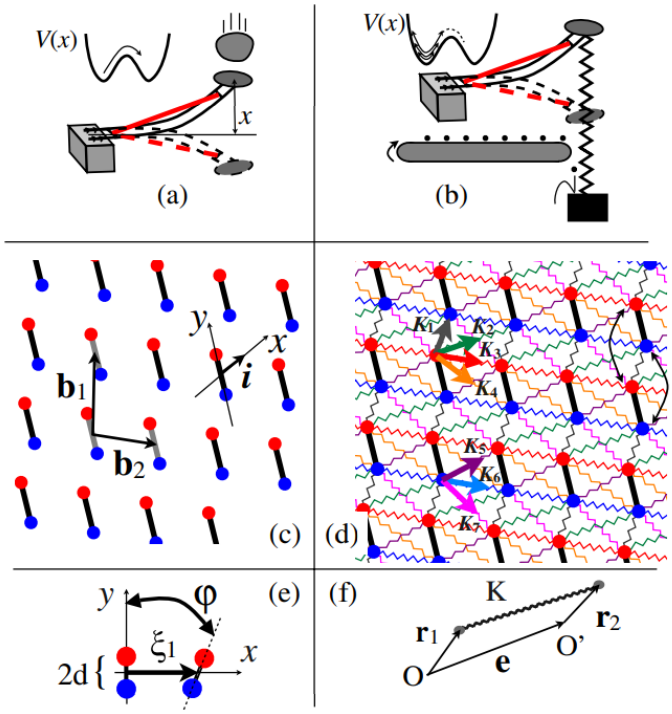

Figure 1.1 A device with a similar energy landscape. The system can be switched between two equilibrium configurations by: **a.** delivering a large amount of energy at once or **b.** by attaching a spring and weight, and releasing the beads one by one. **c.** The 2D lattice of dimers of primitive vectors b_1 and b_2. At equilibrium, the dimers are all parallel and orientated along an arbitrary direction. The *xy* coordinate system indicates the plane of motion. The *y* axis is along the dimer but the *x* axis is arbitrary. **d.** The interaction between the tubulin dimers is modeled by a network of springs. There are 7 distinct springs and corresponding **e** unit vectors. We also indicate second order neighbors whose harmonic interaction is also considered. **e.** The degrees of freedom for the *xy* planar motion. **f.** Stretched configuration of a spring with the ends displaced by r_1, r_2.
Source: [Prodan and Prodan, 2009]

1.2 Microtubules: The Possible Phononic Analog of Topological Insulator

Microtubules are cylindrical protein structures that play a vital role in the cellular architecture and mechanical properties of cells. Composed of tubulin proteins, microtubules form part of the cytoskeleton, providing structural support and contributing to cell shape. Despite their slender dimensions, with an outer diameter of 25 nanometers and lengths of a few microns, microtubules exhibit exceptional stiffness. Their unique mechanical properties are critical for various cellular processes, including cell division. (Figure 1.2)

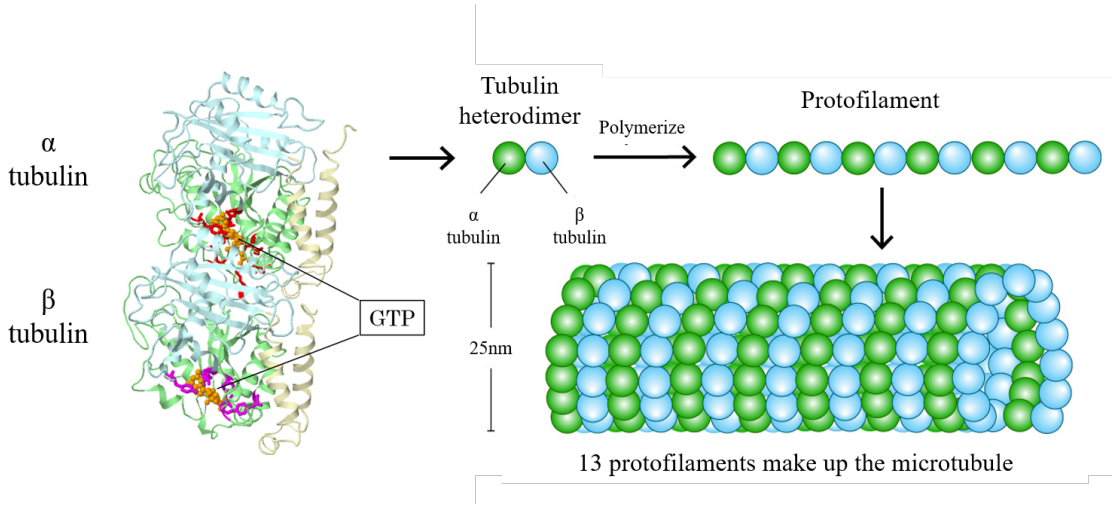

Figure 1.2 Tubulin dimers compose the microtubule. The microtubule is composed of a dimeric structure, where alpha and beta tubulins come together to form a dimer. These dimers then assemble into protofilaments, and a group of 13 protofilaments arrange themselves to create a sheet. The sheet further closes up to form a tubular structure.
Source: [Löwe et al., 2001]

The growth and shrinkage of microtubules occur through the addition and removal of tubulin proteins at their ends. As new tubulin proteins attach, microtubules elongate, while shedding portions of their protofilaments — a filamentous arrangement of polymerized tubulins — results in shortening. Remarkably, microtubules can assemble and disassemble without introducing defects throughout their lifetime, remaining stable in aqueous environments. This dynamic behavior, characterized by the random timing and length of growth and shrinkage, is known as dynamic instability. It is considered a stochastic process due to its unpredictable nature [Fygenson et al., 1994].

In a previous study [Mahadevan and Mitchison, 2005], the total energy of a tubulin sheet was examined with respect to its transversal and longitudinal curvatures near the edge. It was proposed that the energy landscape exhibited two distinct minima separated by an energy barrier. One minimum favored a cylindrical shape, while the other favored a trumpet shape. This sliding motion from one minimum to the other led to the opening of the microtubule ends and subsequent depolymerization. To illustrate a similar energy landscape, consider the device depicted in Figure 1.1. It consists of a bow made of two elastic roads connected by two connectors, with a stretched rubber band between them that can freely slide. The energy of the bow, as a function of the position denoted by x , as shown in Figure 1.1**a**, exhibits two minima. Switching between these minima can be achieved by applying a strong force to the free end or by utilizing a series of low-energy actions. Based on the assumption that topological phonon states can appear at the microtubule's edges, it is highly probable that topological edge modes contribute to the dynamic instability of microtubules [Prodan and Prodan, 2009].

Anticancer drugs can modify dynamic instability. Taxol, an chemotherapy drug commonly used in microtubule studies, plays a role in stabilizing microtubules by binding to them and preventing their disassembly. By disrupting the dynamic instability of microtubules, Taxol effectively inhibits the proper division of cancer cells, making it a valuable treatment option [Jordan and Wilson, 2004]. The presence of just one Taxol molecule per thousand tubulins is remarkably effective in stabilizing the entire microtubule structure, underscoring the profound impact of small structural changes on microtubule behavior [Derry et al., 1997].

Interestingly, Taxol does not appear to significantly affect the static mechanical properties of microtubules. For instance, the range of persistence lengths, which indicates the stiffness of microtubules, remains similar for both Taxol-stabilized and non-stabilized microtubules [Hawkins et al., 2010]. Previous research suggests that Taxol interferes with

the dynamical characteristics of microtubules, giving rise to a new understanding of their dynamic instability [Prodan and Prodan, 2009].

To investigate the small local changes along microtubules and their potential modulation of dynamic instability, we propose utilizing dynamic correlation matrices, which will be discussed in detail in Chapter 2. These matrices provide a means to explore the relationships between neighboring small regions within microtubules, shedding light on the underlying dynamics of these intricate structures.

Resistance to Taxol in cancerous cells has been linked to the production of different isotypes of tubulin, leading to changes in the bulk structure of microtubules and alterations in their dynamic properties [Derry et al., 1997] [Orr et al., 2003]. Previous studies have indicated that cancerous microtubules exhibit slower dynamics compared to regular microtubules [Feizabadi and Rosario, 2017, Newton et al., 2002]. In our research, we investigated the mechanical properties of cancerous microtubules by calculating their persistence lengths and mapping their phonon spectra. The results clearly demonstrated that cancerous microtubules possess distinct mechanical characteristics.

In Chapter 2, we utilized correlation matrices to examine the local differences within individual microtubules. By segmenting the microtubules, we observed random regions of bright and dark fluorescence, representing normal and cancerous tubulins, respectively (Figure2.7). The correlation matrices revealed that the dark regions exhibited greater mechanical flexibility compared to the highlighted segments.

Collectively, these studies have emphasized the importance of exploring the local variations in microtubules, such as Taxol binding and tubulin composition, and their impact on dynamic properties, in the pursuit of effective cancer treatments. The preliminary findings and comparisons between cancerous and regular microtubules are presented in Chapter 2.

1.3 Nanofluidic Devices

To investigate how local changes in tubulins within a microtubule affect its overall properties, we aim to map the complete spectrum of microtubule vibrations, known as the phonon spectrum. The edge modes we seek to identify may occur at high frequencies ranging from 1 MHz to a few GHz. To achieve such frequencies, we require a more confined and controlled environment for the microtubules, which can be accomplished using nanofluidic devices. While nanofluidic devices have been developed for DNA and microtubules in previous studies, our focus is on designing a device specifically for actuating a single microtubule, necessitating a unique and precise design. The device fabrication process involves several steps outlined below.

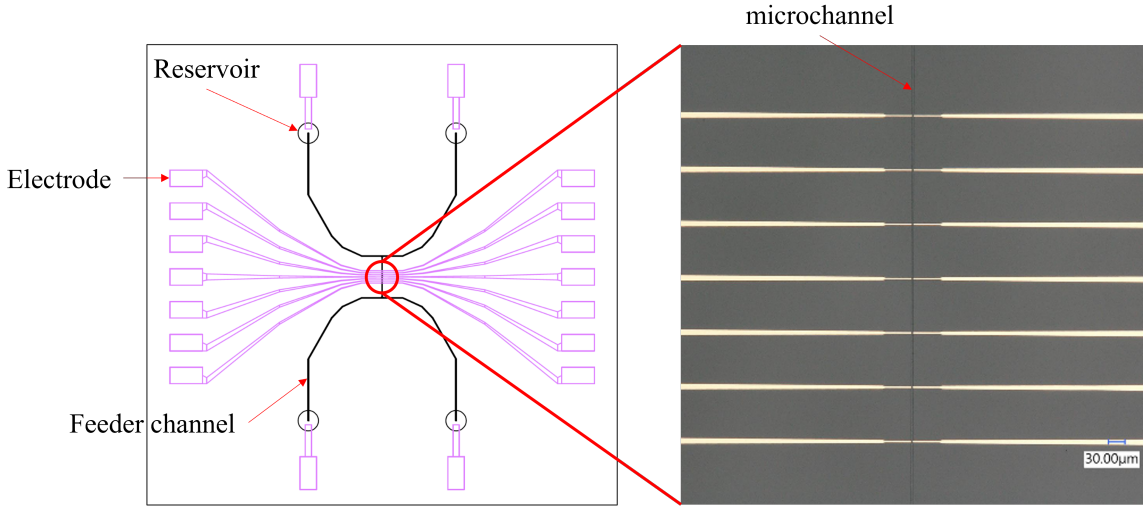

Figure 1.3 Microfluidic device for testing. Left: Schematic representation of the microfluidic device layout. The microchannel contains seven pairs of electrodes positioned on both sides, enabling precise control over the microtubule manipulation. The microtubule sample can be introduced into the device from the reservoirs. Right: The microchannel width is 1.5 micrometers, while the narrowest part of the electrodes measures 2 micrometers in width.

Firstly, we need to create a device with appropriate dimensions for the feeder channels and nanochannels. Due to the rigid nature of microtubules, successful flow of microtubules into the nanochannels presents practical challenges. Careful consideration of the channel dimensions (width and depth) and their intersections is crucial. The nanochannel should be wide enough for microtubules to flow through while preventing rotational movement.

Secondly, our objective is to develop a device with only one nanochannel. Previous attempts yielded devices with approximately 7-20 nanochannels, but for this study, we aim to fabricate a device that allows the study of one microtubule at a time. Ensuring optimal liquid flow within a single nanochannel presents challenges, as the ratio of the cross-sectional areas of the micro-nanochannel and channel bending curvature can significantly affect liquid flow resistance. We plan to optimize the electrophoresis technique to drive microtubules through the nanochannels, determining the ideal voltage for a device with a single nanochannel.

Lastly, we intend to incorporate electrodes into the device to actuate the microtubule. Pairs of electrodes will be positioned along the nanochannel, alternating their voltage at different frequencies. However, the deposition of high-resolution nanoelectrodes using electron beam lithography is a costly and time-consuming process, often requiring multiple trials due to the challenges associated with electrode patterning and alignment. As an alternative plan, we propose exploring different techniques to embed electrodes with sufficient precision.

Through the stepwise development of this nanofluidic device, we aim to create a controlled environment that enables the actuation of a single microtubule and the mapping of its phonon spectrum, ultimately shedding light on the relationship between local changes in tubulins and the properties of larger microtubule assemblies.

1.4 Acoustic Metamaterials

Acoustic metamaterials are engineered structures that possess unique properties resulting from their macroscopic design. By carefully manipulating the structure of these materials, the propagation of sound waves can be controlled and modified to achieve macroscopic material parameters that are not readily attainable in traditional materials. For instance, the frequency range at which sound is absorbed by the material can be precisely controlled by designing the acoustic resonator's structure [Yang et al., 2017]. And acoustic diode can rectify sound waves like current flow of electrical diode [Liang et al., 2009]. There are

other research directions of acoustic metamaterials including acoustic focusing [Al Jahdali and Wu, 2016], acoustic imaging [Zhu et al., 2011], acoustic tweezers [Shi et al., 2009], etc. Our specific research focus lies in exploring a relatively new application of acoustic metamaterials known as topological acoustic metamaterials. These materials serve as the acoustic counterpart to topological materials in condensed matter physics. By employing innovative designs in acoustic metamaterials, we aim to investigate topological phenomena that are challenging to observe in the realms of mathematics and condensed matter physics. The study of topological properties in materials aims to identify inherent properties that remain unchanged in the presence of external forces. This immutability holds significant value for practical applications.

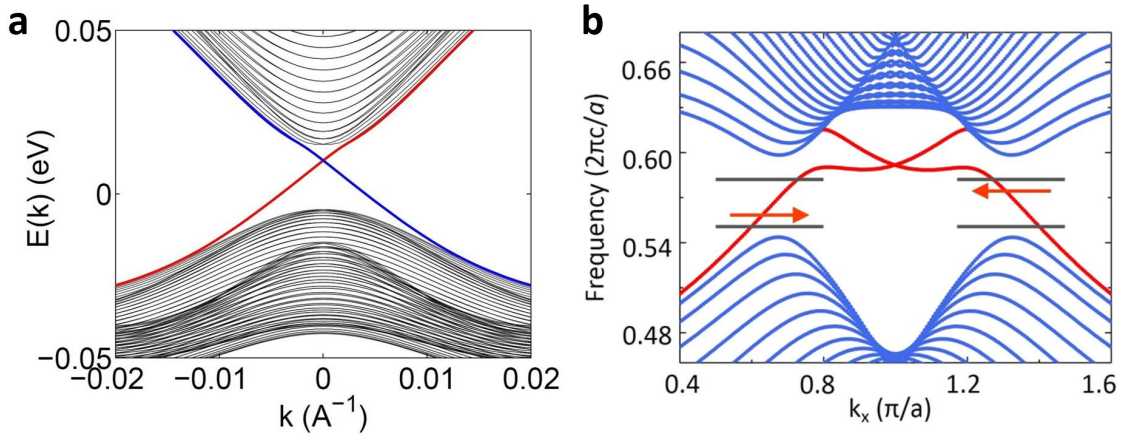

Figure 1.4 Energy spectrum of topological insulator. **a.** There are gapless edge states on the left and right edge (red and blue lines, respectively). **b.** Acoustic one-way edge states. Dispersion of the one-way acoustic edge states (red curves) occurring in a finite strip of the acoustic lattice. The left and right red curves correspond to edge states localized at the bottom and top of the strip.
Source: [Qi and Zhang, 2011a]

Topological insulators are a specific class of materials characterized by their unique band structures, discovered by Shou-cheng Zhang [Qi et al., 2008] and others in quantum wells composed of HgTe and CdTe. A key characteristic of topological insulators is that their internal energy bands exhibit topological triviality, similar to regular insulators, while their surface features a topologically non-trivial energy band structure. This disparity arises

from the crystal boundary's interruption of the electron's periodic potential. Figure 1.4 illustrates the combination of these energy bands.

Within the material (depicted by the black energy bands), the valence band is completely occupied by electrons, rendering it an insulator. On the boundary, we observe the blue and red energy bands, representing the edge states [Qi and Zhang, 2011a]. Notably, these bands connect the conduction and valence bands, allowing electrons occupying these energy levels to be easily accelerated by external electric fields, resulting in a macroscopic current. As a result, the surface of a topological insulator exhibits conductivity. Additionally, due to the dispersion of the boundary states, electrons acquire momentum in limited directions upon acceleration, leading to unidirectional conductivity in two-dimensional scenarios. This remarkable behavior is a hallmark of topological insulators, which possess highly stable boundary states protected by topology, unaffected by impurities.

If we introduce such topological properties to acoustic systems, then we can get topological acoustic metamaterials. Topological insulators, often referred to as symmetry-protected topological phases of matter, exhibit their distinctive properties due to the presence of symmetries. These gapped phases rely on the global nature of their band structures, making the surface states impervious to local perturbations and preserving their topological properties. The characterization and classification of topological insulators and their surface states heavily depend on the dimensionality of the material and the symmetries it possesses. A comprehensive framework known as the periodic table of topological insulators has been established for this purpose [Chiu et al., 2016a].

From an experimental standpoint, it is important to engineer structures that satisfy the required symmetries, as the preservation of symmetry is synonymous with preserving the topological properties. Careful consideration must be given to the choice of coupling methods in topological acoustic experiments in order to maintain the desired symmetries and accurately explore the associated phenomena. In Chapter 4, we will present an effective

and efficient approach for coupling acoustic resonators from the bottom, leading to the preservation of chiral symmetry.

In Chapter 5, we present direct observations of topological phenomena in acoustic crystals without bulk band gaps, providing a general experimental technique to demonstrate their underlying topology. Our findings include the identification of robust boundary-localized states in a topological acoustic metal, as well as the reinterpretation of a composite operator derived from the problem's K-theory. By implementing a physical Hamiltonian based on this composite operator, we directly observe a topological spectral flow and measure the associated topological invariants. These observations and experimental protocols have the potential to shed light on the exploration of topological behavior in a wide range of artificial and natural materials that do not possess bulk band gaps.

CHAPTER 2

MEASURING LOCAL CHANGES IN STRUCTURAL PROPERTIES OF A SINGLE MICROTUBULE

In this chapter, we utilized dynamic correlation matrices to analyze the stiffness of microtubules and uncovered a significant difference between regular and cancerous microtubules. Our findings revealed that cancerous microtubules exhibit higher flexibility, which may be caused by the alterations in their structural integrity. By capturing the subtle variations in stiffness along the microtubule structure, this approach provides valuable insights into the mechanical properties of microtubules, with potential implications for targeted interventions in cancer research.

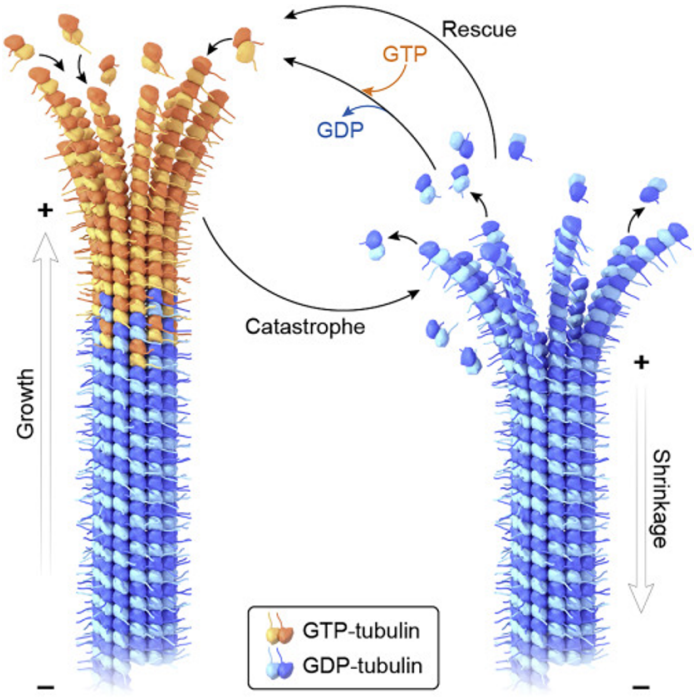

Figure 2.1 Dynamic instability of a microtubule. The microtubule is composed of a dimeric structure, where alpha and beta tubulins come together to form a dimer. These dimers then assemble into protofilaments, and a group of 13 protofilaments arrange themselves to create a sheet. The sheet further closes up to form a tubular structure. Despite its narrow width of 25nm, the microtubule exhibits remarkable stiffness.
Source: [Roll-Mecak, 2020]

2.1 Introduction

A microtubule is a cylindrical structure composed of tubulin proteins, characterized by an outer diameter of 25 nanometers and a maximum length of up to 100 micrometers. One of the remarkable properties of microtubules is their ability to undergo dynamic instability, a process where they exhibit spontaneous changes in length. This phenomenon has been observed both in laboratory settings (in vitro) and within living cells, suggesting that it arises from the inherent interactions among the constituent proteins and the overall structure of the microtubule itself [Fygenson et al., 1994, Lange et al., 1988, Martin et al., 1991, Desai and Mitchison, 1997, Hyman et al., 1992, Derry et al., 1997] What makes microtubule dynamic instability fascinating is the seemingly unpredictable transition between growth and shrinkage, commonly referred to as rescue and catastrophe, as illustrated in Figure 2.1. Unlike predetermined limits, microtubules can elongate or contract to varying extents, adding to the complexity of this process. A widely accepted theory proposes that the GTP "cap", the orange part in Figure 2.1, potentially plays a role in stabilizing the microtubule. If the GTP-tubulin molecules in the cap hydrolyze rapidly, exposing GDP-tubulin, the microtubule disassembles. On the other hand, "rescue" occurs when new GTP-tubulin molecules attach to the end of the microtubule, replenishing the GTP cap. [Desai and Mitchison, 1997]

We are confronted with a fundamental inquiry: What is the impact of local structural modifications within the microtubule on its macroscopic property of dynamic instability? Our simplified representation of the microtubule structure has left significant gaps in our comprehension of the underlying mechanism driving dynamic instability, consequently widening our knowledge deficit regarding chemotherapy drug resistance. The GTP cap theory falls short in explaining the sporadic disappearance of the GTP cap and how a small GTP cap can effectively maintain the cohesion of microtubule with varying lengths. The disassembly of the microtubule lacks a discernible critical length or time threshold, and

the precise mechanism by which subtle alterations in microtubule structure finely regulate dynamic instability remains elusive.

However, it is clear that even subtle changes in the structure of the microtubule's building blocks have noticeable effects on the dynamics at the ends of the microtubule. Could these local modifications alter the overall energy landscape of the microtubule? [Mahadevan and Mitchison, 2005] proposed that microtubules behave as a bistable system, with energy minima favoring polymerization and depolymerization, separated by an energy barrier that must be overcome to transition between the two phases. When tubulin proteins bind to the growing microtubule, they hydrolyze GTP and release 12.5 kcal/mol, which could potentially provide the necessary energy to surpass this barrier. However, the factors that determine the prevalence of the growing phase over the catastrophe phase and the underlying mechanism of the transition point are still not well understood.

An alternative mechanism was proposed by [Prodan and Prodan, 2009] for the microtubule to accumulate enough energy within its structure to overcome the energy barrier and initiate the shortening of the microtubule. Theoretical calculations of the vibrational energies of microtubules revealed intriguing properties, suggesting that they can function as topological phononic insulators. As a result, the structural characteristics of microtubules inherently create a phononic energy gap—a range of frequencies that can induce external vibrations without transferring energy through the material. Notably, within this energy gap, there exists a singular energy state known as an edge mode. At specific frequencies within the energy gap, the bulk of the material does not transmit energy, while the edges exhibit amplified vibrations. Theoretical analyses further indicate that microtubules possess edge modes capable of storing significant amounts of vibrational energy at their tips. This discovery provides a potential explanation for the energy source driving the transition from a growing microtubule to a shrinking one.

Cancerous microtubules may have slow dynamic comparing with regular microtubules. [Newton et al., 2002] [Feizabadi and Rosario, 2017] Measuring the persistence

length of a polymerized material allows us to quantify the stiffness. From the data we have from tracking the movement of microtubules, we then applied the analysis method from [J. Nettleton, 1993] [Hawkins et al., 2012] to calculate the persistence lengths of cancerous and regular microtubules. Considering that cancerous microtubules have different isotypes of tubulins from regular microtubules, their mechanical properties may vary.

To further investigate the changes occurring along the microtubules, our objective is to examine the stiffness matrices of regular microtubules and cancerous microtubules with different concentrations of Taxol. Additionally, we plan to analyze the matrices of segmented microtubules, which will provide insights into any local variations.

2.2 Theoretical Considerations

To study the phonon spectrum and local properties of microtubules, we developed our own techniques since existing methods were not readily available. Our methodology involved growing microtubule samples in a solution and stabilizing them with taxol. By capturing a thousand frames of video and utilizing the ImageJ plugin, we tracked the movement of the microtubules. To accurately represent the microtubule's structure, we modeled it as a chain of interconnected beads resembling a polymer, where each bead had distinct interactions with its neighbors. Figure 2.2 Segmenting the microtubule into individual beads allowed us to monitor their positions over time, enabling a thorough analysis of the impact of local variations on the overall behavior and properties of microtubules. This innovative approach provided valuable insights that closely align with the real characteristics of microtubuleS.

We can derive a correlation matrix by considering the displacements of each bead or the bending angles between beads, which captures the interdependency among them. This statistical method enables us to analyze the relationships between any two random variables, specifically the movement of beads in the microtubule. Unlike methods assuming uniformity among pairs, this approach accommodates the measurement of varying stiffness

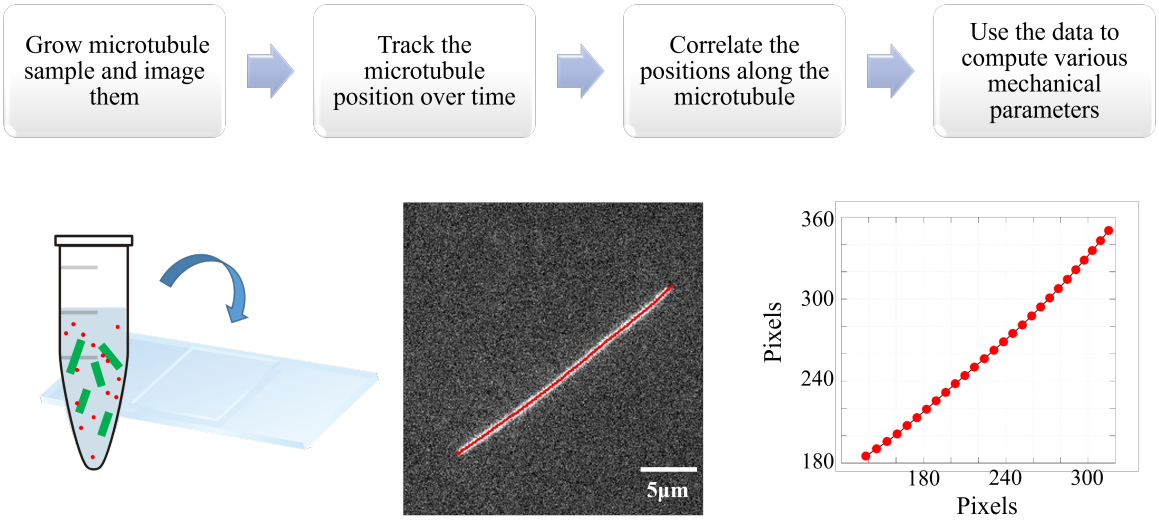

Figure 2.2 Experimental Workflow for Studying Microtubule Properties. Left: Growing microtubule samples in a solution and stabilizing them with taxol. The prepared sample was then placed on a slide and covered with a glass cover for imaging. Middle: Capturing a thousand frames of the microtubule and tracking the movement with ImageJ software. Right: Divide the microtubule into beads to study the local interaction from their movement.

along the microtubule. These variations may arise from taxol attachment or the distribution of different tubulin isotypes.

Suppose you get the position of the beads at each time t:

$$u_n(t), n = 1, \ldots, N, \quad t \in [0, T] \ . \tag{2.1}$$

Here N is a number of beads.

The dynamic correlation matrix is defined as the displacement of pairwise beads from an equilibrium position over time:

$$C_{i,j} = \langle u_i u_j \rangle_t = \lim_{t \to \infty} \frac{1}{t} \int_0^t u_i(s) u_j(s) ds, i, j = 1, ..., N \tag{2.2}$$

The stiffness matrix is then derived from

$$C = k_B T K^{-}1 \rightleftharpoons K = k_B T C^{-}1 \tag{2.3}$$

Imagine a system of a particle with very small mass attached to a soft spring doing Brownian motion in liquid at temperature T. We can write down The potential energy of the mass-spring system $V = \frac{1}{2}Ku^2$, K is the spring constant; the time average of the potential energy should equal the quantum of thermal energy $\left\langle \frac{1}{2}Ku^2 \right\rangle = \frac{1}{2}k_B T$, then we have $K = k_B T \frac{1}{\langle u^2 \rangle}$.

When the system is at thermodynamic equilibrium, the time average of the physical observables, in our case the displacements $u_i(t)$, coincide with their ensemble averages:

$$C_{i,j} = \lim_{t\to\infty} \frac{1}{t} \int_0^t u_i(s)u_j(s)ds = \frac{1}{Z} \int e^{-\beta[T(p)+V(u)]} u_i u_j dp du \tag{2.4}$$

Where $\beta = \frac{1}{k_B}$ and Z is the free energy of the system.

$$Z = \int e^{-\beta[T(p)+V(u)]} dp du = \int e^{-\beta T(p)} dp \int e^{-\beta V(u)} du = Z_p Z_u \tag{2.5}$$

One important observation is that the integrals over p and u decouple in Eq 2.4, and the momentum factors out completely. Hence,

$$C_{i,j} = \frac{1}{Z_u} \int \int e^{-\beta V(u)} u_i u_j du \tag{2.6}$$

With the harmonic approximation $V(u) = \frac{1}{2}\sum_{ij} K_{i,j}u_i u_j$, Eq 2.6 can be evaluated explicitly as

$$C_{i,j} = \frac{1}{Z_u}\int\int e^{-\beta V(u)} u_i u_j du = \frac{1}{\beta}\left\langle K^{-1}\right\rangle_{i,j} \tag{2.7}$$

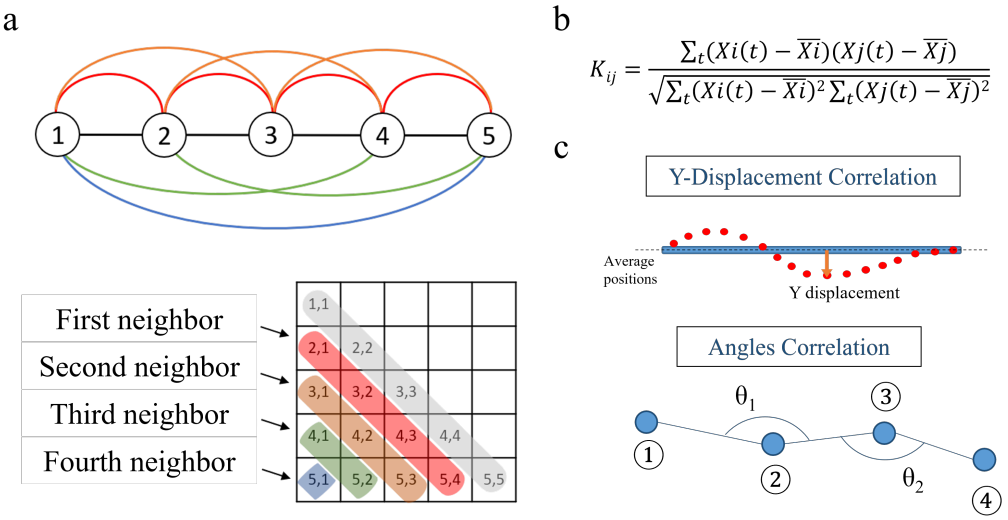

Figure 2.3 Dynamic correlation matrix. **a.** An illustration to show how the correlation matrix is constructed. The diagonal elements of the correlation matrix represent the correlations of each bead with itself and hold no information. The off-diagonal elements, however, provide insights into the correlations between beads and their neighboring beads. For example, the second diagonal reflects the correlations between a bead and its immediate neighboring bead, the third diagonal represents the correlations between a bead and its second neighboring bead, and so on. **b.** The general equation for calculating elements in correlation matrix. **c.** Illustrations for Y-displacement correlation and angle correlation. A negative correlation value indicates that neighboring beads within the microtubule are moving in different directions, indicating a bending region and implying greater flexibility in that particular area.

As long as the damping is only a direct function of the momentum (velocity) of the particle, which is the case in most situations, the relation between dynamic correlation matrices and stiffness matrices remains the same because the momentum will factor out [equations (2.4) and (2.6)]. Thus, we can extract the natural frequencies of an undamped system from a damped system, such as microtubules in buffer.

2.3 Preliminary Work

In our previous study [Aslam and Prodan, 2019], we accomplished the mapping of phonon spectra for naturally vibrating microtubules. Building upon this research, we are now motivated to investigate whether the phonon spectra of cancerous microtubules present distinct variations in comparison to regular microtubules. Through this exploration, we aim to gain insights into the potential differences in mechanical properties between cancerous and regular microtubules. Preliminary observations suggest that cancerous microtubules demonstrate greater flexibility, as evidenced by their phonon spectra (Figure 2.4). This finding highlights the significance of studying the phonon spectra as a means to unravel the mechanical characteristics of microtubules affected by cancer.

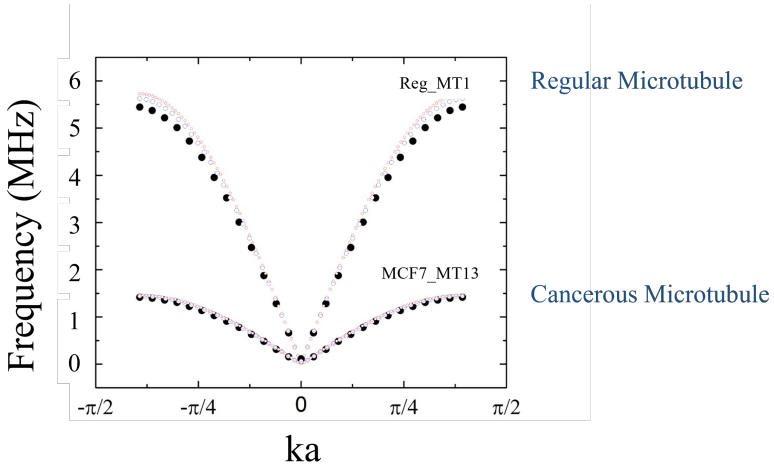

Figure 2.4 Phonon Spectra Comparison of Regular and Cancerous Microtubules. The phonon spectra of regular and cancerous microtubules reveal distinct characteristics. The regular microtubule exhibits a steeper slope, indicating a faster group speed of the sound wave and implying a stiffer material. In contrast, the cancerous microtubule displays a flatter slope, indicating greater flexibility.

We calculated the persistence lengths of 11 MCF-7(breast cancer cell line) cancerous microtubules, the average of them is 0.3559 ± 0.3562 mm, it is one order less comparing to the persistence lengths of regular microtubules from our previous work 2.20 ± 1.74 mm. The result also shows that cancerous microtubules are mechanically more flexible.

The comparison of correlation matrices of a regular microtubule and a cancerous microtubule can be seen in Figure2.5. We divide the microtubule into 101 beads, and in

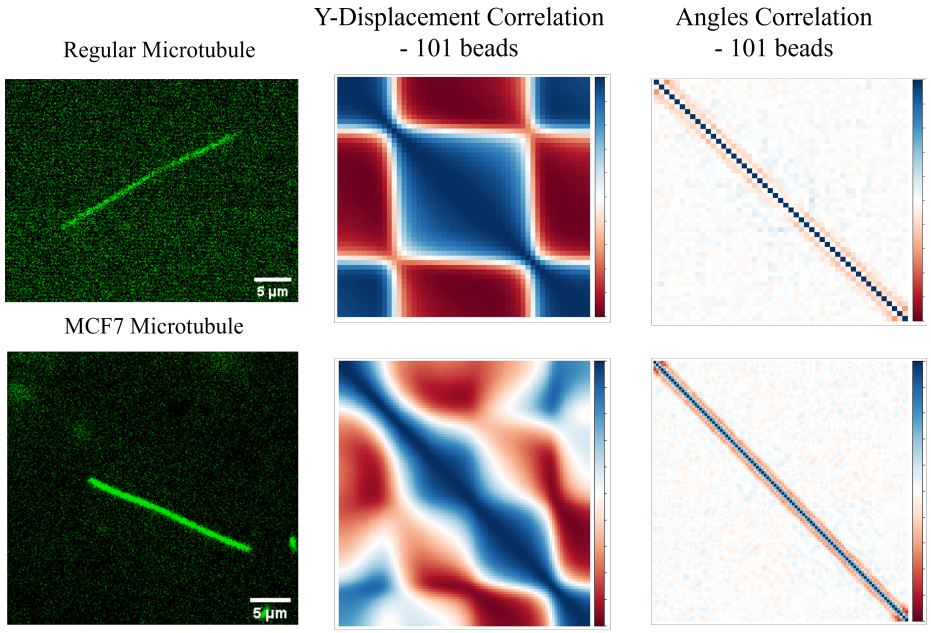

Figure 2.5 Correlation matrices show that regular microtubule is more rigid than a cancerous microtubule. Top left: A regular microtubule. Top middle and right: Correlation matrix of Y-displacements and angles of regular microtubule. Bottom left: A cancerous microtubule. Bottom middle and right: Correlation matrices of Y-displacements and angles of cancerous microtubule.

the correlation matrices of Y-displacements, color blue means positively correlated, color red means negatively correlated. For the regular microtubule, we can see in Figure2.5 that it is highly correlated between beads even they are quite far apart from one another; and for the cancerous microtubule (MCF-7) it reflects the low correlation along the microtubule. The result is in agreement with the values of their persistence lengths, indicating that the cancerous microtubules are indeed less stiff. However, in Figure2.6, after doubling Taxol concentration, the correlation matirx of cancaerous microtubule started to look like a regular one; which means Taxol molecules binding change the stiffness. The segmented cancerous microtubule in Figure2.7 also supports the same argument; it was consist of 11% fluorescence labeled regular tubulins and 89% unlabeled MCF-7 cancerous tubulins, the dark joints where red arrows point at in Figure2.7 were consequently made of mostly cancerous tubulins. The correlation matrices of the segmented microtubule shows a very good correspondence: the dark segments are less correlated.

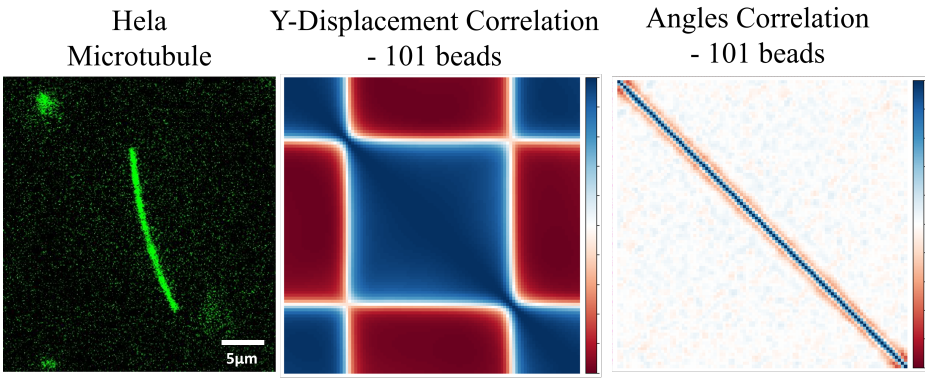

Figure 2.6 Taxol rescues the rigidity of cancerous microtubule. Left: A cancerous microtubule with double Taxol concentration. Middle: Correlation matrix of Y-displacements. Right: Correlation matrix of angles.

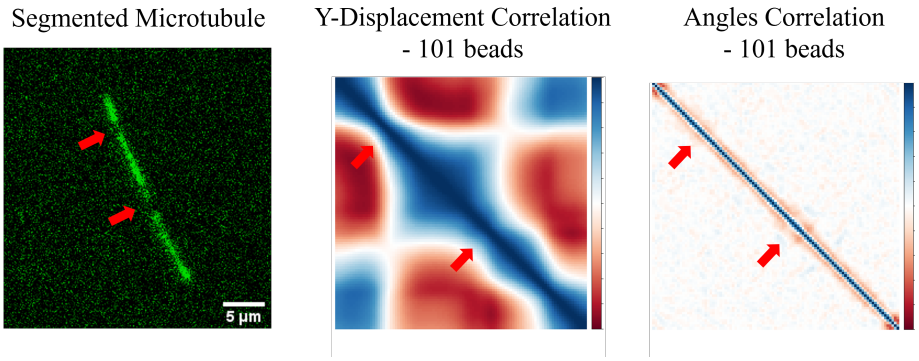

Figure 2.7 Correlation matrices can pinpoint the local rigidity of a microtubule. Left: A segmented cancerous microtubule. Middle: Correlation matrix of Y-displacements. Right: Correlation matrix of angles.

2.4 Experimental Protocols

2.4.1 Grow microtubules

Regular microtubules Purchased from PurSolutions, pure double cycled tubulin and tubulin labeled with Alexa488 and Alexa594 were stored in -80°C in PEM buffer (80 mM piperazine-N,N'-bis2-ethanesulfonic acid(PIPES), 1 mM ethylene glycol tetraacetic acid (EGTA), 1mM MgCl2, pH 6.9).

To grow microtubules, the tubulin was thawed on ice and grown in a GPEM buffer (1 mM guanonine triphosphate (GTP), 80 mM PIPES, 1 mM EGTA, 1mM MgCl2, pH 6.9) with 10% dimethyl sulfoxide (DMSO). The solution was incubated on ice for 5 minutes and then incubated at 37°C for one hour. The tubulin was grown at 2 mg/ml with 10% to 50% labeled tubulin. After incubation, warm Taxol was added to a final concentration of 10 M. The stabilized microtubules were diluted 100 times in an anti-bleaching solution (250 nM glucose oxidase, 64 nM catalase, 40 mM D-glucose, 1 beta-mercaptethanol (BME)) before imaging.

Samples for imaging were prepared by coating the glass slide and coverslip with bovine serum albumin(BSA), dropping 1.5-2 μl of the diluted microtubule solution onto the slide, and sealing the coverslip to the slide with one minute epoxy.

Cancerous microtubules Same as above, except the tubulins are consist of 11% labeled regular tubulins and 89% unlabeled cancerous tubulins. For growing segmented cancerous microtubules, simply add two kinds of tubulins into solution without pipetting them.

2.4.2 Image microtubules

A Prime $95B^{TM}$ Scientific CMOS Camera was used to acquire videos of the microtubules at 10-100 frames per second. The plug in JFilament in FIJI was used to find the initial coordinates of the microtubule. The ends of the microtubule can easily move out of focus, and this results in missing data points in the tracking. Therefore, only microtubule that

stayed in focus for 1000 frames were used for analysis to ensure that the length of the tracked microtubule did not change significantly over time.

2.4.3 Image analysis

The coordinates from JFilament were then fit to a spline in MATLAB, and segmented into 27, 51, or 101 equal length blocks. Each block is represented by the position of its center of mass. We utilized Fortran to extract the Y-displacements and angles data, and then incorporated R Program for computing the correlation matrices.

2.5 Conclusion

Up until this stage of our research, the observed vibrations of microtubules were primarily induced by the thermal energy present in the surrounding water. As a result, we were limited to observing the lower vibrational modes of the microtubule. To gain a comprehensive understanding of the complete phonon spectrum, it becomes imperative to excite higher vibrational modes of the microtubules. In order to achieve this, we have devised two distinct plans.

The first plan involves tethering microtubules with fluorescent beads and employing piezoelectric devices to induce controlled vibrations. By precisely actuating the microtubules using this approach, we aim to access a broader range of vibrational modes and subsequently map out the full phonon spectrum. This method provides us with a means to manipulate the vibrational behavior of the microtubules and gain insights into their unique vibrational properties.

The second plan revolves around the creation of a well-controlled environment, specifically utilizing nanofluidic chips equipped with electrodes along the sides. By subjecting a single microtubule to this controlled setup, we can stimulate its vibrational modes with greater precision. This approach allows us to create a highly controlled

experimental system that facilitates the excitation and analysis of specific vibrational modes within the microtubule.

Both plans aim to expand our understanding of the vibrational characteristics of microtubules by enabling the exploration of higher vibrational modes and mapping out the complete phonon spectrum. By implementing these strategies, we can uncover valuable insights into the unique vibrational properties of microtubules and further investigate their potential as topological phononic insulators.

CHAPTER 3

ISOLATING A SINGLE MICROTUBULE IN NANOFLUIDIC DEVICE

This work is available as an arXiv preprint with the identifier arXiv:2302.08433.

Biological systems have been theoretically predicted to support topological wave-modes, similar to the ones existing in meta-materials. The existing methods to measure these modes are not implementable to biological systems; new techniques have to be developed to accommodate measurements in life science. Motivated by this perspective, we report a nanofluidic device for studying one microtubule at a time. Micro-channels etched into fused-silica using reactive ion etching were interfaced with nanochannels milled with electron beam lithography, and sealed with a PDMS-coated glass coverslip. The microchannels are 1 μm deep and 100 μm wide, and the nanochannels are 150 nm deep and 750 nm wide, they are tested to be effective for isolating microtubules. The methods presented here are for an adaptable nanofluidic platform for phonon measurements in biopolymers made of proteins or DNA.

3.1 Introduction

The field of topological mechanics and metamaterials is expanding to incorporate soft topological materials, such as micro and nano scale colloids and polymers, including biopolymers, suspended in water based media [Prodan and Prodan, 2009, Prodan et al., 2017]. Phenomena similar to the one seen in topological insulators, like Thouless pumping, are theoretically proposed to exist in polymers suspended in fluids. In particular the the microtubules and actin have been proposed to support topological phonon modes [Prodan and Prodan, 2009], and has been inspiring the development of other lattices [Prodan et al., 2017]. While the bending modes of the microtubules have been experimentally measured, the rest of the modes requires confinement and precise actuation [Aslam and Prodan, 2019]. Previous experimental methods to obtain of the density of state of colloidal micro-particles

in suspension require accurate tracking of particle for a long period of time [M. F. Islam, 2010]. To adapt such methods to microtubules, one needs to confine the microtubules to stay in the field of view of the microscope for a longer time, while allowing them to exibit dynamic instability. The development of techniques in nanofabrication has become an increasingly useful tool in the life sciences [Cao et al., 2002, Öz et al., 2019, Yeh et al., 2015, Kutchoukov et al., 2004, C. Iliescu, 2012, Cannon et al., 2004, Xia et al., 2008]. Methods that are developed for nanofluidic channels are adaptable for microscopy and can integrate electronics for sensing and actuation of single proteins or macromolecules. [Reisner et al., 2012, Kaji et al., 2004, Wang et al., 2005] Single proteins and macromolecules are typically imaged at high magnification using fluorescence or bright-field microscopy. This requires imaging through a thin optically transparent material, typically glass or fused-silica. Furthermore, the ability to adapt nanofluidic devices for electrodes to incorporate manipulation and sensing requires the nanochannels to be in an insulating material, and this is another benefit to fabricating in glass or fused-silica.

In this paper we present a method for confining a single microtubules in a nanochannel and a highly repeatable and detailed method for interfacing microchannels that are 50 μm apart with 750 nm wide by 150 nm deep nanochannels and capping them with a glass coverslip using PDMS as a bonding medium. The bonding is done outside the cleanroom and does not require expensive equipment. [Haubert et al., 2006] The nanochannels are written into fused silica using electron beam lithography (E-beam lithography or EBL). This device can be used for transmission and fluorescence microscopy at high magnification with low fluorescence background. This method can be adapted to include electrodes in the nanochannels for sensing and actuation with dimensions that promote high signal to noise ratio.

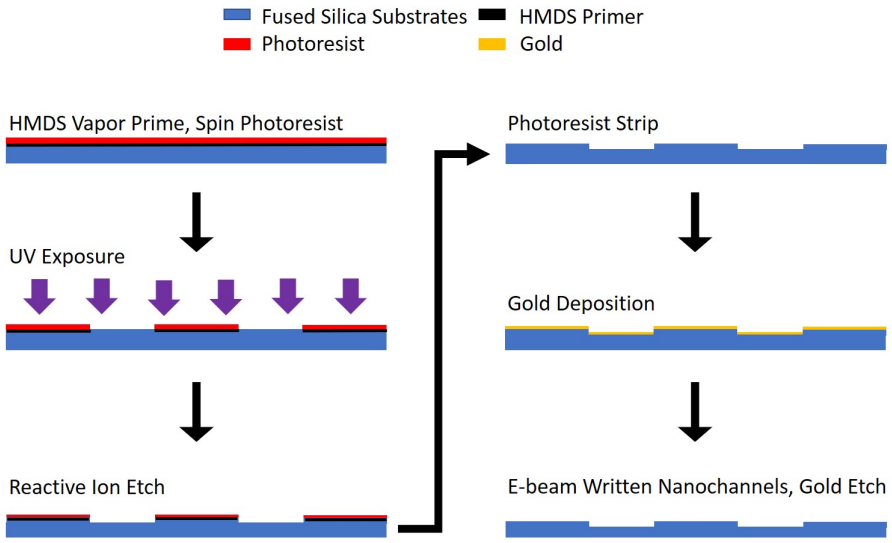

Figure 3.1 Cross-sectional nanochannel process flow. Directions of steps indicated by arrows. First, start with an HMDS vapor primed fused-silica wafer coated in 1.8 μm AZ1518 photoresist. Next, perform UV photolithography exposure with indicated photomask. RIE exposed pattern to etch it into the substrate. Strip wafer in microposit remover 1165 photoresist stripper at 70°C. This allows microchannels of width, $w = 50\mu$m, and depth, $d = 1.5\mu$m to be present on substrate. Prepare wafer with 15 nm gold for E-beam writing. Gold etch after the nanochannel pattern is written.

3.2 Fabrication of Nanofluidic Devices in Fused Silica

3.2.1 Fabrication of microchannels

The devices were fabricated on 500 μm thick fused-silica wafers with a diameter of $d = 76.2$ mm. The wafers were cleaned in a Piranha solution 3:1 H_2SO_4:H_2O_2 for 5 minutes, followed by a DI water bath for 1 mintue. The wafers were rinsed with DI water and dried with N_2. Next, the wafers were placed in an isopropyl alcohol (IPA) bath for one minute, followed by a DI water bath for another minute. Afterwards, the wafers were rinsed with DI water and dried with N_2.

Next, the wafers were primed with hexamethyldisilazane (HMDS) in a Yield Engineering Systems (YES) HMDS prime oven at 148°C. The procedure dehydrates the wafers and then vapor primes them with HMDS. Next, AZ1518 positive photoresist was spun on the wafers at 4000 RPM for 40 s. The wafers are baked at 110°C for 2 minutes and then cooled on a cooling plate. Standard photolithography was performed for 30 s using a

EVG620 mask aligner to expose the sample with the microchannel pattern shown in Figure 3.2. The wafers were manually developed in AZ300 MIF for 60 s.

Wafers were measured with a Bruker Dektak-XT profilometer to verify that the photoresist was properly removed from the patterning area. Next, the wafers were placed in an Oxford PlasmaPro 80 Reactive Ion Etch (RIE) and an O_2 descum was run for 2 minutes to remove any residual resist from the microchannel structure due to exposure and development. Next, an SiO_2 etch was performed for 15 minutes. The etch is a combination of CF_4 and O_2 gasses at 35 sscm and 3 sscm, respectively. The set forward power was 300 W and the DC bias was between 520 and 530 V. The wafers were measured with the profilometer to verify the etch depth. The photoresist was stripped for 1 hour in Dow Microposit Remover 1165, and the final depth of each channel was measured once more in the profilometer. The final depth of microchannels was around 1 μm.

In order to prep the fused-silica substrates for E-beam lithography, E-beam resist was spun on the wafers before they were coated in 15 nm of gold in an Angstrom Nexdep E-beam evaporator.

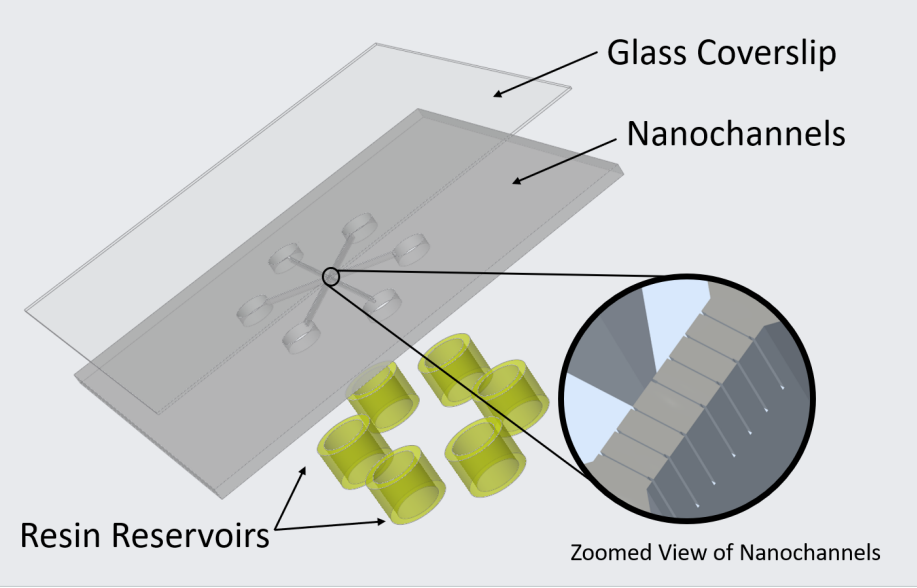

Figure 3.2 Rendered CAD model of the microchannel device integrated with the nanochannels. Nanochannels are highlighted by the zoomed view insert. Imaging is done through the glass coverslip with an inverted microscope.

3.2.2 Electron-beam written nanochannels

The pattern of nanochannels were designed to be cascading to guide microtubules in Figure 3.3**a,b**. Nanochannels were written between the microchannels using the Elionix ELS-G100, an electron-beam lithography system with high speed and ultra high precision thermal field emission. The ELS-G100 is capable of writing and generating patterns with a line width of 6 nm. One wafer was loaded into the FIB chamber at a time. The SEM with a beam current 500 pA was used to focus on the sample surface to determine the z-axis working distance and locate the writing area on the sample. After focusing the beams on the wafer, the pattern of nanochannels were aligned and then the wafer was ready to be exposed.

After E-beam lithography, wafers were developed in 70% cold IPA and then inspected under microscopy to confirm that the pattern was well-written. A gold etch was then performed on the samples to remove the Au coating. Next, the wafers were placed in RIE again to etch the nanochannels with calculated parameters until the depth reached 150 nm (Figure 3.3**d**). The E-beam resist was stripped for 1 hour in Dow Microposit Remover 1165. Next, the wafers were again coated with AZ1512 photoresist to be diced into 20 mm x 20 mm devices, and transported to the lab for bonding.

3.2.3 Packaging fluidic devices

Port holes were made at the ends of the microchannels using a BNP 220 Suction Blast Cabinet. The metal mask was made beforehand and the devices were fixed and protected by 3M Scotch Magic Tape.

To seal the devices, a modified PDMS bonding protocol was performed. To prepare for the sealing of the nanofluidic devices, it is critical that the bench top, fume hood, and laminar flow hood be as clean and dust-free as possible. They are all cleaned with 70% ethanol and again with IPA. A Ni-Lo 4 XL vacuum holder digital spin coater is cleaned,

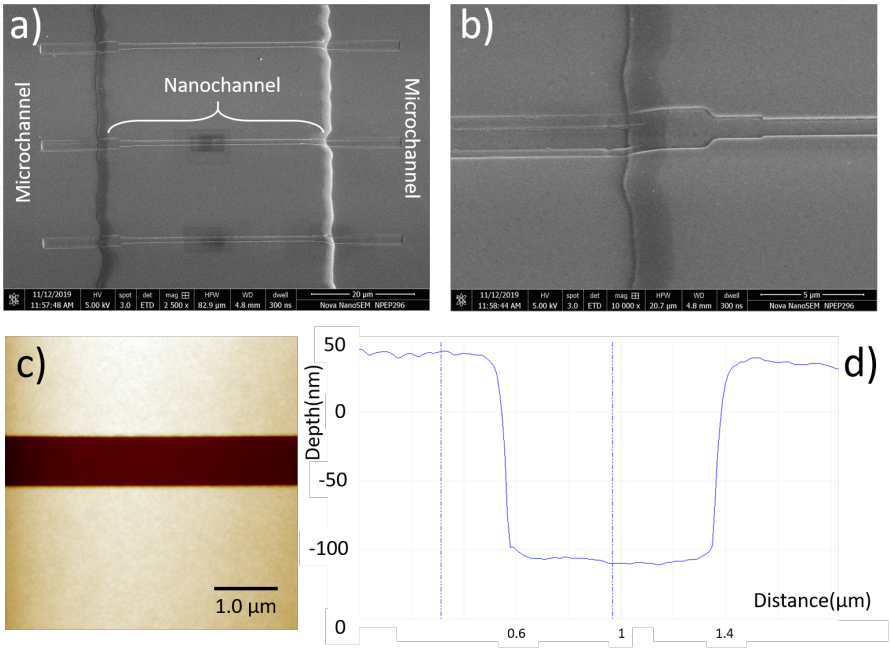

Figure 3.3 SEM and AFM characterization. **a.** SEM image of microchannels integrated with nanochannels. **b.** 10000x magnification of the cascading junction between the micron-sized and nano-sized channels. **c.** AFM image of one nanochannel. **d.** The measured depth of the nanochannel is around 150 nm.

lined with fresh foil and set to 3 stages of spinning: 500 RPM for 10 s, 3000RPM for 30 s, and 5000 RPM for 20 s. The speed was reached with 500 RPM ramp speed.

Photoresist is stripped from the diced devices with 1165 microposit remover for 15 minutes at 70°C before the bonding procedure begins. The devices and 22 mm x 22 mm coverslips are cleaned by placing them in a chemically resistant coverslip rack and sonicating them in acetone for 5 minutes. Devices and coverslips are rinsed in the rack sequentially with acetone, IPA, ethanol, and DI water.

PDMS (SYLGARD 184 Silicone Elastomer Kit, Dow Corning) was mixed with its curing agent in the volume ratio of 10:1, then the mixture was placed in a desiccator for an hour to remove the bubbles. Next, 500 μl bubble-free PDMS was spun on per coverslip, coated coverslips were then moved to a pre-heated 120°C hot plate, and cured for at least an hour.

Both the device (patterns face up) and coverslip (PDMS side up) were placed side by side in laminar flow hood, and treated with BD-20AC laboratory corona treater for 5 minutes. After corona treatment, the device was flipped and carefully placed on the coverslip, the bonding should happen consequently, if not, use the blunt side of a tweezers to gently tap the device on the corner. After the devices were sealed, 4 resin reservoirs were adhered to 4 ports using Loctite Epoxy instant glue, after the Epoxy was cured, the devices were ready for use.

3.2.4 Flowing microtubule into nanochannels

All the steps below have to be done in a humidity chamber that can be made from an empty pipette tip rack with 2 Kimwipes soaked with DI water inside. The devices should sit on the rack and the lid should be closed during waiting to prevent the device from dehydration.

The channel has to be first rinsed with PEM buffer (80 mM piperazine-N,N'-bis2-ethanesulfonic acid (PIPES), 1 mM ethylene glycol tetraacetic acid (EGTA), 1mM MgCl2, pH 6.9). 15-20 μl PEM buffer was pipetted into one port on the left microchannel, the nanochannels began filling up with liquid within 15 minutes; the excess solution from the port was pipetted out, then another 15-20 μl was placed at the port of the right microchannel. This step is to create fluid pressure for the liquid to flow in. The device was let sit in humidity chamber for another 15 minutes until all channels were filled up.

The channels then have to be passivated with BSA to prevent the adhesion of microtubules to the surface. 10 μg/ml bovine serum albumin (BSA) diluted in PEM buffer was flowed into the device. 15-20 μl BSA was pipetted into one port on the left microchannel, then waited 30 minutes for BSA to fill up the left part. The excess solution was pipetted out from the port. Another 15-20 μl was added at the port of the right microchannel. After adding the solution, the device was let sit for another 30 minutes for the channels to be filled up.

To test the quality of the seal, 1 mM fluorescein solution diluted in PEM buffer was flowed into the device. Fluorescein is sensitive to blue light, so solutions were made in with red or yellow light and foil was used to cover any containers to prevent bleaching of the sample before imaging. The nanochannels were imaged at 100x magnification with a 1.6x optovar to increase magnification. The fluorescein solution flowed into the nanochannels by placing 15-20 μl solution at one port on the left microchannel, the nanochannels began filling up with liquid within 15 minutes; the excess solution from the port was pipetted out, then another 15-20 μl was placed at the port of the right microchannel, and another 15 minutes was give for the device to sit in the humidity chamber until all channels were filled up.

Pure double cycled tubulin and tubulin labeled with Alexa594 (Red) were stored in -80°C in PEM buffer. To grow microtubules, the tubulin was thawed on ice and grown in a GPEM buffer (1 mM guanonine triphosphate (GTP), 80 mM PIPES, 1 mM EGTA, 1mM MgCl2, pH 6.9) with 10% dimethyl sulfoxide (DMSO). The solution was incubated on ice for 5 minutes and then incubated at 37°C for one hour. The tubulin was grown at 2 mg/ml with 10% to 50% labeled tubulin. After incubation, warm Taxol was added to a final concentration of 10 M. The stabilized microtubules were diluted 100 times in an anti-bleaching solution (250 nM glucose oxidase, 64 nM catalase, 40 mM D-glucose, 1 beta-mercaptethanol (BME), 10 μM Taxol) before flowing into fluidic devices.

We found that electrophoresys works best at guiding microtubules from the ports into the nanochannel. Electric field of 0.9 V/m was applied using a DC power supply, it took 15-30 minutes until the microtubules approached the nanochannels.

The cleanliness of the wafer is critical for each stage of the process. Any particulates on the surface can block the fluidic channels or cause an uneven photoresist deposition. Wafers that were not cleaned properly at each step did not have precise patterning of the microchannels due to uneven photoresist, and this caused jagged edges on the microchannels.

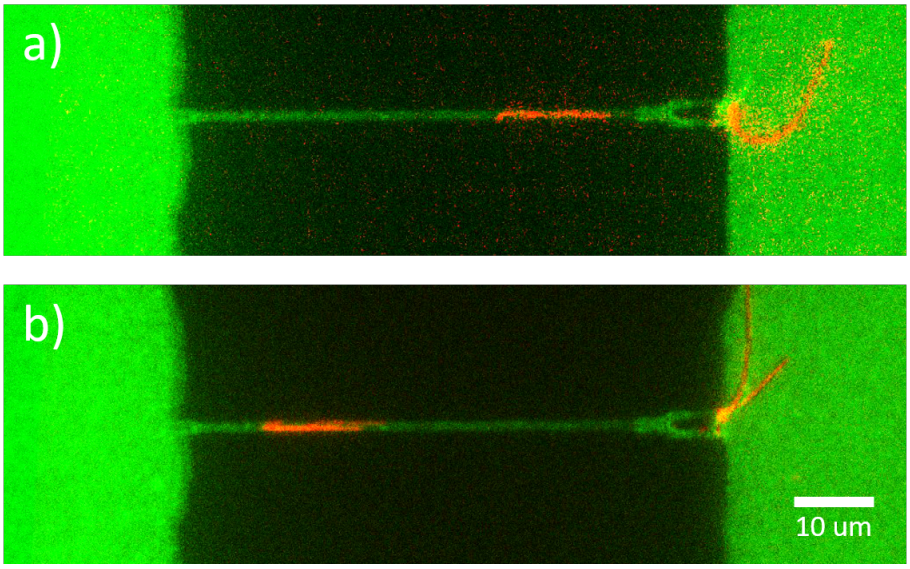

Figure 3.4 Microtubule in nanochannel. Image of one fluorescence labeled microtubule(red) moving in the nanochannel filled with 1 mM fluorescein solution(green) at 100x with fluorescent microscope. **b.** was taken 50 millisecond after **a**.

Photoresist also does not adhere well to fused-silica. Priming the wafers with HMDS was a necessary step to promote the adhesion of the photoresist to the wafers.

The profilometer measurements are important to verify proper photoresist development, the etch rate of the RIE, and the final depth of the microchannels. Photoresist AZ1518 is 1.8μm in depth, and the profilometer measurement after the photoresist was developed verified that the photoresist is removed from the microchannels and the wafer is set for etching. The RIE etch process etches both the fused-silica and the photoresist with different selectivity, so the etch time for a specific depth must be determined. The wafers are etched for different times, and profilimeter measurements are performed for each time to determine the etch rate. An etch time of 1 hour and 15 minutes resulted in a 1.2 μm deep microchannel.

The gold coating on the samples is necessary for SEM imaging. Fused-silica is non-conductive, and therefore charging effects due to the SEM makes it difficult to image. Charging occurs when the electrons do not have a conductive path to guide them away from the sample surface and a layer of electrons is generated. The cloud of electrons prevents

clear projectile of the secondary electrons from the surface to the electron detector, resulting in poor image quality. The gold coating provides a conductive path the the electrons to move away from surface during imaging. However, long exposure to the electron beam still resulted in charging effects.

The E-beam lithography was done on one wafer (12-21 devices depends on their size) at a time. The process is achieved by shooting a focused electron-beam at the surface of the material. The system provides a stable 1.8 nm electron-beam using high beam current at 100 kV, it is accurate and highly efficient. After exposure, the depth of nanochannels can be decided by how long they are etched in RIE.

The bonding process is robust, repeatable, and easily done outside of the clean room. A successful bonding can be seen by eye by a change in contrast between the coverslip and the fused-silica. The drawback of this method is that the sagging of PDMS material tends to partially or completely seal off the channels that do not have a high aspect ratio due to the rubber-like behavior of PDMS. However, it was noticed that if PDMS coated coverslips were let cool down after one hour heat treat and wait overnight, the chance of PDMS collapse and block the channels becomes slim.

The port holes used to be made by drilling into the ends of the microchannels using a drill press at 3600 rpm using a diamond coated drill bit of 0.5 mm diameter. The drilling of the port holes can be difficult as well as time consuming, and still result in cracking the device. Sandblasted-through portholes have cleaner edges, and the sizes of holes are well-controlled by the metal masks, also portholes of a dozen of devices can be done within a few minutes.

3.3 Results and Discussion

Previous devices for studying microtubule are microns in size. [Yokokawa et al., 2005, van den Heuvel et al., 2007]. The depth of our channels is 150 nm and was chosen to keep the microtubules in the field of view of a microtscope for longer while still allowing space

for dynamic instability. The width of the nanochannel is 750nm and was chosen to allow future actuation of the microtubule in the nanochannel for the purpose of exiting different types of vibrational modes in the microtubules lattice.

Microtubules have a persistance length of 1mm making them much stiffer and longer than DNA. We found that electrophoresis was the best way to guide the microtubules into the nanochannels. We previously tried flow, and kinesin, a motor protein, but without success. For this step to be successful, it is very important that the bonding is airtight such that the electric field goes primary through the nanochannel. The width of the microchannel has to be large to allow the microtubules to align with the electric field prior to the entrance in the nanochannel.

In Figure 3.4, we present a microtubules flowing, under electric field through our nano channels. Prior to the flow we test the bonding and wether the channel is free by flowing flourescein (green) into the nanochannel. The microtubule (red) is flown through the nanochannel using electric field. The position of the microtubule can be controlled. This method can be further adapted to embed electrodes on two sides of the nanochannels for sensing and actuation.

3.4 Conclusion

In conclusion, isolation of a microtubule in a 150 nm deep nanochannel is reported. The channel is well characterized using SEM and AFM. The method to seal the fluidic channels allows for easy imaging with a microscope. This methodology allows for an adaptable tool to isolate a single microtubule to perform direct and quantitative measurements. The reported device is further adaptable to fabricating electrodes along the channel as an added sensor to detect and measure in the nanochannel. The small dimensions of the nanochannel are crucial for the addition of electrodes because to increase the signal to noise ratio the electrodes need to be close enough to the object of study to minimize electrical signal from the solution itself.

The use of nanofluidic platforms has already benefited the study of DNA's unique structural properties. The adaptability and repeatability of the fabrication of the devices presented here makes it an ideal platform to open the doors to isolate and study not only DNA, but also other proteins and protein assemblies. For example, the nanochannels can be milled to an ideal height and width to isolate single actin or microtubule proteins. These biopolymers have unique polymerization and depolymerization properties that need to be quantitatively measured at the protein level to elucidate the dynamic mechanics of these structures. This platform allows for variations in size that can be optimized for the object of study. Furthermore, this platform affords the ability to isolate and manipulate macromolecules and proteins for measurements, while keeping their naturally aqueous environment.

In our research, we have successfully developed a nanofluidic device that allows us to isolate a single microtubule. This achievement marks a significant milestone in our quest to explore the vibrational properties of microtubules at a more controlled and precise level. With the nanofluidic device in place, our next step is to integrate electrodes into the setup.

By incorporating electrodes along the sides of the nanofluidic device, we will have the means to induce controlled vibrations in the isolated microtubule. This capability opens up exciting possibilities for mapping the phonon spectrum of the microtubule with greater accuracy and detail. The electrodes will enable us to selectively excite specific vibrational modes and explore the full range of vibrational behaviors exhibited by the microtubule.

The addition of electrodes to the nanofluidic device represents a crucial advancement in our experimental setup, as it empowers us to manipulate and analyze the vibrational properties of the microtubule in a controlled environment. This step will pave the way for in-depth investigations into the unique vibrational characteristics of microtubules and their potential as topological phononic insulators.

Overall, our progress in constructing the nanofluidic device for isolating a single microtubule sets the stage for the subsequent exploration of the microtubule's vibrational

landscape through the incorporation of electrodes. This advancement brings us closer to unraveling the mysteries of microtubule phonon spectra and their potential as topological phononic insulators.

CHAPTER 4

SYMMETRY-PRESERVING COUPLING METHOD FOR TOPOLOGICAL ACOUSTIC METAMATERIALS

This work is available as an arXiv preprint with the identifier arXiv:2303.06065.

In this chapter, we investigate different types of couplings used in acoustic metamaterials requiring preservation of symmetries. For testing we use the SSH model to test whether topologically edge and interface modes are supported with the different types of connection. We observed that a modular platform where the resonators are coupled through the bottom is the simplest method that is accurate and flexible.

4.1 Introduction

Topological insulators have attracted significant interest due to their distinct characteristics, setting them apart from metals and insulators. [Hasan and Kane, 2010a]. In recent years, the topological state of bosons (photon [Ozawa et al., 2019a] and phonons [Zhang et al., 2018a]) has also attracted great attention.

The field of topology has paved the way for the realization of novel mechanical and acoustic systems. Particularly, phononic crystals have emerged as a captivating subject, as they present exciting prospects for manipulating sound in unconventional and unexpected manners, leveraging the principles of topology.

Periodic acoustic systems, such as the topological boundary states based on the analogue of quantum Hall effect [Khanikaev et al., 2015, Yang et al., 2015], the analogue of quantum spin Hall effect [He et al., 2016], the Floquet topological insulator [Peng et al., 2016], and the valley Hall effect [Lu et al., 2016] have been successively proposed and experimentally verified. Besides periodic systems, topological systems that lack periodicity can also achieve topological edge states, such as topological quasi-crystals [Ni et al., 2019a, Cheng et al., 2020a, Apigo et al., 2019a, Coutant et al., 2021] where the topological

structure is caused by disorder. The idea of topological acoustic insulators provides new schemes for designing devices with advanced functionalities. For example, the potential improvement of leaky-wave acoustic antenna [Fleury et al., 2016], directional topological acoustic antenna controlling sound for versatile applications [Zhang et al., 2018b], specific signal filtering achieved by adding random disorder to clean structures. [Zangeneh-Nejad and Fleury, 2020], various sound proof strategies [Yamamoto et al., 2009, Xu et al., 2020, Liu et al., 2021], and for a growing discussion of different fractal geometries. [Song et al., 2016, Zhao et al., 2018, Singh et al., 2022] In essence, researchers have been and continue to intensely explored various topological acoustic systems, and among these researches, topological acoustic meta-material consisting of numerous phononic crystals is one of the focuses.

In view of the fact that topological insulators are also called symmetry-protected topological phases of matter, these gapped phases have topological properties relying on the presence of symmetries. This result is from a global property of the topological insulator's band structure: local perturbations cannot alter or damage this surface state. Since the properties of topological insulators and their surface states highly depend on the dimension of the material and its symmetries, they can be categorized using the periodic table of topological insulators [Chiu et al., 2016a]. From the experimental perspective, it is crucial to satisfy certain structures and to display the symmetry, moreover, preserving the symmetry is equivalent to preserving the topological properties. To preserve symmetry, coupling methods for topological acoustic experiments must be carefully chosen. The following question then arises: in discrete acoustic resonant models, how can the resonators be efficiently coupled to form a desired structure while preserving the symmetry so that it complies with the idea of topological metamaterial?

Some methods preserve the symmetry using double side connection, meaning they added a coupling bridge that is also on the side and made the structure symmetric [Zheng et al., 2022, Xiao et al., 2017, Ma et al., 2019, Qi et al., 2020]. The resonators are 3D

printed using photosensitive resins or other types of materials as coupling bridges must be fabricated with the resonators which makes as manufacture more complicated and time consuming. On top of that, if the dimension of the coupling bridge has to be changed, everything has to be made from scratch all over again.

In this section, we test an acoustic coupling method to connect the resonators through the bottom to preserve the symmetry and create a simple, flexible and Lego-like platform. We will compare two types of coupling methods throughout the paper: side coupling and bottom coupling (Figure 4.1**b**). We will start by showing that bottom coupling preserves symmetry in simple periodic acoustic models while single side coupling fails to do so. Via the simulations of resonant modes of dimer, trimer, pentamer, and a classic Su–Schrieffer–Heeger model (SSH model) consisting of 14 resonators, as well as another SSH model with 28 resonators and a domain boundary. Furthermore, we address the corresponding experimental results of the dimer, the SSH model, and the SSH model with a domain boundary. All experimental results clearly show great agreement to the simulations, proving the effectiveness and simplicity of bottom coupling method.

4.2 Results and Discussion

The dimensions of the resonators that were used throughout the simulations and experiments are shown in (Figure 4.1**a,b**).

4.2.1 Side connection vs. Bottom connection

To demonstrate and to compare the effect of side connection and bottom connection for topological acoustic resonators, numerical simulations were done using COMSOL Multiphysics software.

The simulated results is reported in Figure 4.1 where the structures of dimer, trimer and pentamer of resonators with both side bridge coupling and bottom bridge coupling (Figure 4.1**b**). The band spectrum (Figure 4.1**c,d,e**) were generated by sweeping the width

of coupling bridge from 1 mm to 20 mm with 1 mm steps and plotting corresponding eigenfrequencies versus widths. The wider coupling bridge means stronger coupling strength. In the band spectrum, the second mode split and the gap became larger when the coupling strength went up. With red dash lines as symmetry axes, it is clear that with side connection, the splitting modes are not symmetrical. Once we moved the coupling bridges to the bottom, the symmetry was restored.

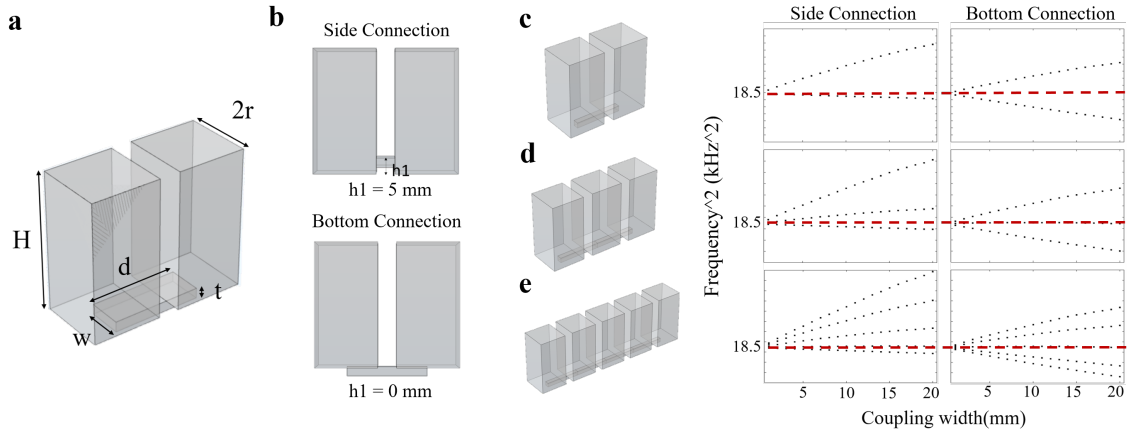

Figure 4.1 Simulations showing that the bottom connection preserves the symmetry. **a.** Dimensions of the resonators and coupling bridges. H = 40 mm, r = 10 mm. The coupling bridge has the width = 5 mm, the length d = 26 mm, the thickness t = 3 mm. **b.** The height position of the coupling bridge h1 = 5 mm for side connection, h1 = 0 mm for bottom connection. **c.** Dimer structure and the band spectrum of both side and bottom coupling methods. **d.** Trimer structure and the band spectrum of both side and bottom coupling methods. **e.** Pentamer structure and the band spectrum of both side and bottom coupling methods. It is clear in the band spectrum that in all three cases, the symmetry is preserved when the resonators are connected through bottom. Red dash lines indicate the symmetrical axis.

4.2.2 Dimer experiment

The experiment of dimer coupling was done to confirm the simulation results. The COMSOL-simulated acoustic pressure fields of the resonant modes are shown in Figure 4.2**e**, the coupling width equals to 5 mm. The assembly process is shown in Figure 4.2**a,b**, and the experimental set up is shown in Figure 4.2**f**. The speaker and the microphone were placed on top of the same resonator to give off and collect sound, respectively. The frequency of the input signal sent to the speaker was swept from 4 kHz to 5 kHz in intervals of 10 Hz.

Experimental results of dimer with bottom coupling bridges show a great agreement to the simulations (Figure 4.2**c**, bottom panel). The middle of 2 peaks is about 4.3 kHz, same as where the 2 modes start to split in the band spectrum (around 18.5 kHz^2). However, with the side connection, the peaks shifted from the spectrum. Additionally, the height difference in peaks for bottom coupling is noticeably smaller than that of the side coupling (Figure 4.2**d**). Comparing with the results from bottom coupling method, the symmetry was distinctly absent for side coupling.

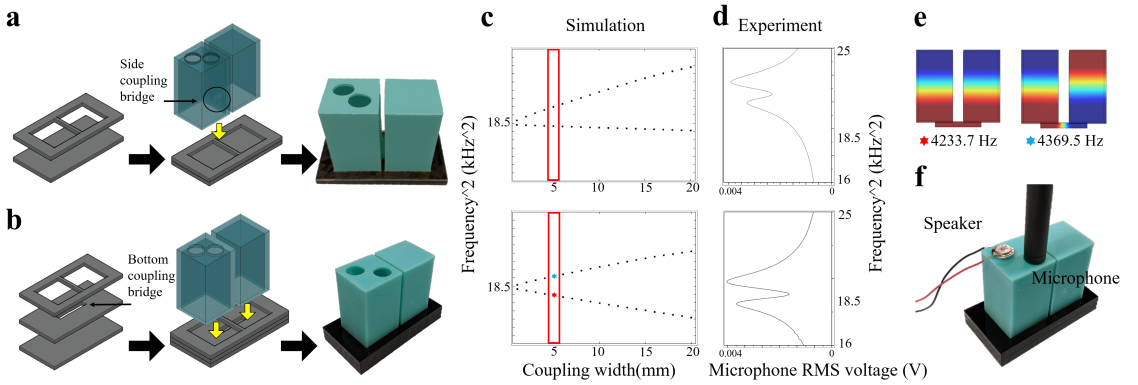

Figure 4.2 Dimer experimental setups as well as the comparison of simulation and experiment results. **a.** Assembly process of dimer connected through side. The dimer was 3D-printed together with a side coupling bridge, the height position of the top of the side coupling bridge h1 is equal to 7 mm. **b.** Assembly process of dimer connected through bottom. Two resonators were 3D-printed separately, and the bottom coupling bridge is grooved in the middle acrylic sheet as depicted. **c.** Simulation results of dimers with side connection (top panel) and bottom connection (bottom panel). Red boxes in both band spectrum indicate the coupling width (5 mm) used in the experiment. **d.** Experimental results of dimers with side connection (top panel) and bottom connection (bottom panel). The symmetry is lacking for side coupling in both simulation and experiment. **e.** Acoustic pressure field distribution for the modes marked as red and blue dots in panel **c.** when S = -5 mm. **f.** The experimental setup.

4.2.3 SSH acoustic model

To further explore how the position of connection between acoustic crystals would influence topological gaps in band spectrum, we started by simulating 3 types of connection for SSH model of 14 resonators. The first type is to couple them with bridges connected through side, the second one is double side coupling bridges, and the third one is bottom connection.

Figure 4.3**a** shows the top view of SSH coupling bridges. r_1 and r_2 are the widths of coupling bridges, therefore they are related to the alternate coupling strength. Light blue dash lines indicate where the resonators were placed. The geometries of 3 coupling types are shown in Figure 4.3**b, c, d**. The resonant spectrum were generated by sweeping S – half of the difference in widths between strong and weak coupling bridge – from -9 mm to 9 mm. When S equals to zero, all coupling bridges have an identical width of 10 mm.

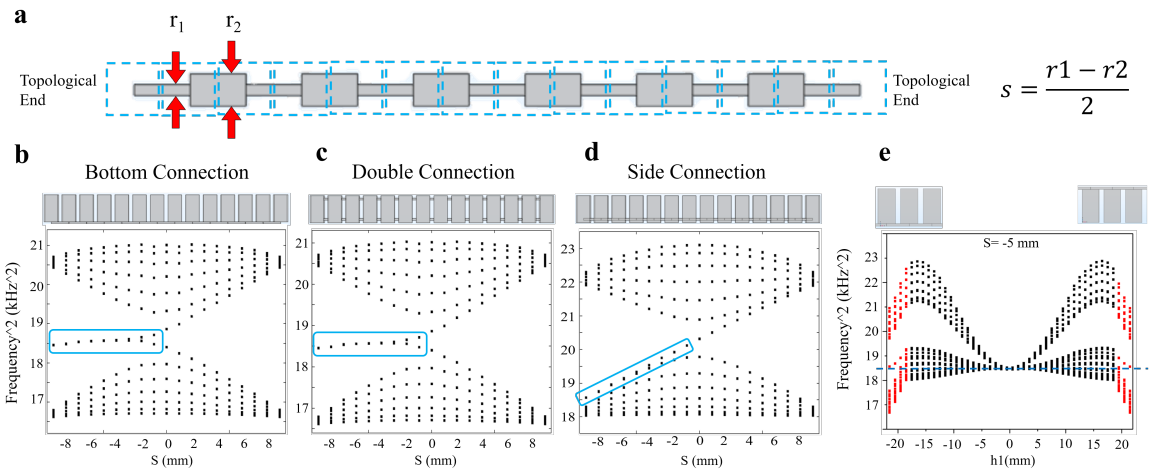

Figure 4.3 Band spectrum of different types of connection in SSH model of 14 resonators, sweeping S. S is half of the difference in widths between strong and weak coupling bridge. **a.** Top view of SSH coupling bridges. r_1 and r_2 are related to the alternate coupling strength. Light blue dash lines are where the resonators were placed. **b.** SSH model with bottom connection. **c.** SSH model with double connection from the sides. **b.** and **c.** has very similar spectrum. Blue boxes include edge resonant modes. **d.** SSH model with side connection, the edge band merges into bulk. **e.** Band spectrum of SSH model sweeping the height of the coupling bridges. Red parts represent when the coupling bridges protrude from the bottom or top. Dark blue dash line marks 18.5 kHz^2.

As one can see in the spectrum (Figure 4.3**b, c, d**, there is no gap for a uniform coupling connection (S = 0 mm, r_1 = r_2 = 10 mm). A bulk spectral gap opens once the connecting channels are set in an alternating strong/weak coupling strength ($S \neq 0\ mm$). Furthermore, the bulk spectrum remains symmetric with respect to the middle of the bulk spectral gap (the small deviations are less than 5% when compared with the overall width of the bulk spectrum).

In (Figure 4.3**b**), SSH model with bottom connection, one can observe the expected edge resonant modes, whose energies are pinned in the middle of the bulk spectral gap

around 18.5 kHz^2, where the second mode of resonant frequency of a single resonator is. We can say that SSH model with bottom connection, COMSOL-simulated spectra displays an exact chiral symmetry. In Figure 4.3**c**, SSH model with double side coupling bridges gives the same spectra, meaning both types of coupling approaches achieve the goal of protecting the chiral symmetry.

On the other hand, the spectra of SSH model connected through sides does not display the same symmetry. In Figure 4.3**d**, not only do the edge modes merge into lower bulk bands, but the middle point of the spectrum shifted to around 2 kHz^2, demonstrating the same impracticality as in dimer experiments.

We also checked to see if the height position (h1 in Figure 4.1**b**) of side coupling plays a role in preserving the symmetry. The height of side coupling bridge was swept from bottom to top to generate the spectra in Figure 4.3**e**, while the coupling width were fixed at $r_1 = 15$ and $r_2 = 5$ (S = -5 mm). When h1 = -21.5 and 21.5 mm, the resonators are coupled from the bottom or from the top which resulted in bulk modes symmetric with respect to 18.5 kHz^2, and the edge modes appear at middle. Red parts represent when the coupling bridges protrude from the bottom or the top, meaning part of them are outside of the resonators, there are still edge modes existing in the gap but the symmetry shifts further and further away from the dash line. One can see that once the coupling bridges enter the body of resonators, the edge modes merge into bulk and the symmetry disappears.

Next, we did experiments with SSH model connected through bottom to confirm if the symmetry is also seen in the experimental results. Figure 4.4**a** shows how the setup was made. The COMSOL-simulated acoustic pressure fields of the edge resonant modes are shown in Figure 4.4**b**. The simulated band structure in Figure 4.4**c** is added as a reference (same as Figure 4.3**b**).

In these measurements, same as dimer experiments, the speaker and the microphone were inserted in the same resonator via two holes open at the top and the speaker's frequency was swept from 4 kHz to 5 kHz and the microphone picked up corresponding signals. The

measurements were repeated for all resonators and the collected data was assembled in the local density of states plot shown in Figure 4.4**d**. It is worth mentioning here that all resonators are removable and interchangeable, so the one with holes can be placed at any probe position desired for measurements. Panel **e** provides an alternative depiction of the same data. The spectral gap as well as the expected edge and interface modes can be clearly identified and they are well aligned with the simulation in panel **c**.

The density of states reported in Figure 4.4**d** was obtained by integrating the local density of states acquired from resonators whose index are the same as the position of the probe. The same instrumentation was used. The measurements were repeated while moving the position of the probe. For each measurement, the frequency was scanned from 4 kHz to 5 kHz in 20 Hz steps.

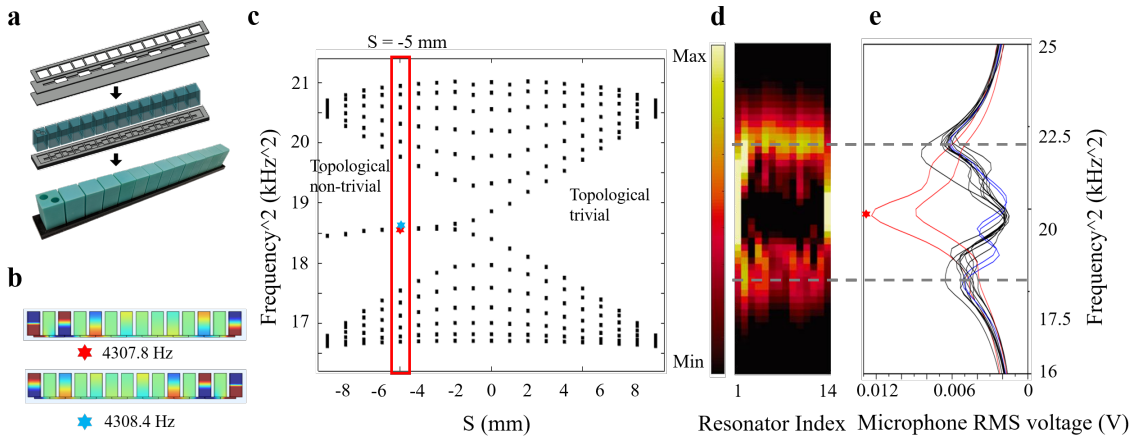

Figure 4.4 SSH experiments demonstrate the simplicity and efficiency of bottom coupling method. **a.** The assembling process of SSH model of 14 resonators connected through bottom. **b.** Acoustic pressure field distribution for the edge modes marked as red and blue dots in panel **c.** when S = -5 mm. **c.** COMSOL simulated SSH model resonant spectrum. The red vertical box indicates S = -5 mm which makes $r_1 = 15$ mm and $r_2 = 5$ mm, the parameters used in the experiments. **d.** Experimentally measured local density of states, assembled from normalized microphone readings from the top of the block resonators. The bright dispersive modes indicate the bulk and edge modes. **e.** Collapse on the frequency axis of the intensity plot in **d.**. The spectral gap is clearly recognized and the edge modes that show up in the gap are marked with a red star.

Finally, we test and compare two coupling methods in a SSH model with a domain boundary(interface), both simulationally and experimentally. A SSH model with a domain

boundary separates two topologically distinct SSH insulating phases, with one non-trivial edge(left) and one trivial(right). It is shown in Figure 4.5**a** where $r_1 = 15$ mm and $r_2 = 5$ mm. Figure 4.5**b** and Figure 4.5**c** show the band spectrum of side connection and bottom connection, respectively. Red vertical boxes include resonant modes when S = -5 mm. Red and blue stars label where interface mode and edge modes appear, and the acoustic pressure field maps are shown below. Similar to the previous results, with bottom coupling, both simulation and experiment verified that the system contains topological resonant modes at the non-trivial edge as well as the domain boundary as expected, and they are located in the middle of the bulk band gap. In opposition, with side coupling, the edge mode disappears and the interface mode is close to the bulk, besides, it is noticeable that the energy is not as concentrated at interface from the acoustic pressure field distribution.

We also did experiments for bottom-connected SSH model with a domain boundary, the same protocol was applied and frequency was swept from 4 kHz to 5 kHz. The measurements were repeated for all 28 resonators and the collected data was then used to plot the local density of states which is shown in Figure 4.5**d**. Panel **e** shows the collapse of the data in panel **d** on the frequency axis. The spectral gap as well as the expected edge modes can be clearly identified and are well aligned with the simulation in panel **c**. The COMSOL-simulated acoustic pressure field maps of the edge resonant modes are shown in Figure 4.5**b, c**.

4.3 Material and Methods

4.3.1 Simulation

The simulations reported in all figures were performed with the COMSOL Multiphysics pressure acoustic module. The wave propagation domain shown in Figure 4.1 was filled with air with a mass density 1.3 kg/m^3 and the sound's speed was set at 343 m/s, which is appropriate for room temperature. We shall consider the 3D printing UV resin material as hard boundary because of the huge acoustic impedance mismatch comparing with air.

4.3.2 Experiment

The resonators were 3D-printed using Anycubic Photon 3D printer, which uses UV resin and has 47 um XY-resolution and 10 um Z-resolution. The thickness of the walls is 2 mm, which ensures a high Q factor and justifies the rigid boundaries in the simulations. The inner dimensions of the resonators are shown in Figure 4.1**a**.

A dimer with a coupling bridge on the sides is 3D-printed as a whole. The width, length and the position of the coupling bridge are as labeled in Figure 4.1**a**. One side was left open for ethanol rinsing and UV-curing. The dimer was then placed on a base of two layers of acrylic plates (top layer: 2 mm in thickness, bottom layer: 3 mm in thickness) to create a closed space for wave propagating (Figure 4.2**a**). The reason that the top layer was 2 mm is to accommodate the side bridge. The bottom connection is achieved by assembling the supporting base, which consists of three layers of 3 mm thick acrylic plates (Figure 4.2**b**). The middle layer of a groove is to account for acoustic coupling. The acrylic plates with patterns of the supporting bases were cut by the Boss Laser-1630 Laser Engraver. The nominal tolerance of the laser-cutter is 250 um.

For the SSH model connected from bottom, the same method was utilized. 14 resonators were placed and coupled through the channels with alternating widths grooved in the acrylic plates of the base. These resonators are detachable and interchangeable so that they can be moved around, thus acoustic crystals with different probe positions can be generated, and the resonators can be taken apart, stored and reassembled for new projects or designs.

The protocol for the acoustic measurements shown in Figure 4.2, Figure 4.4 and Figure 4.5 was as follows: Sinusoidal signals of duration 1 s and amplitude of 0.5 V generated by a Rigol DG 1022 function generator were sent out to a speaker placed in a porthole opened on top of a resonator. A dbx RTA-M Reference Microphone with a Phantom Power was inserted in a porthole next to the previous one and was used to acquire the acoustic signals (Figure 4.2**c**). The signals were then read by a custom LabVIEW code

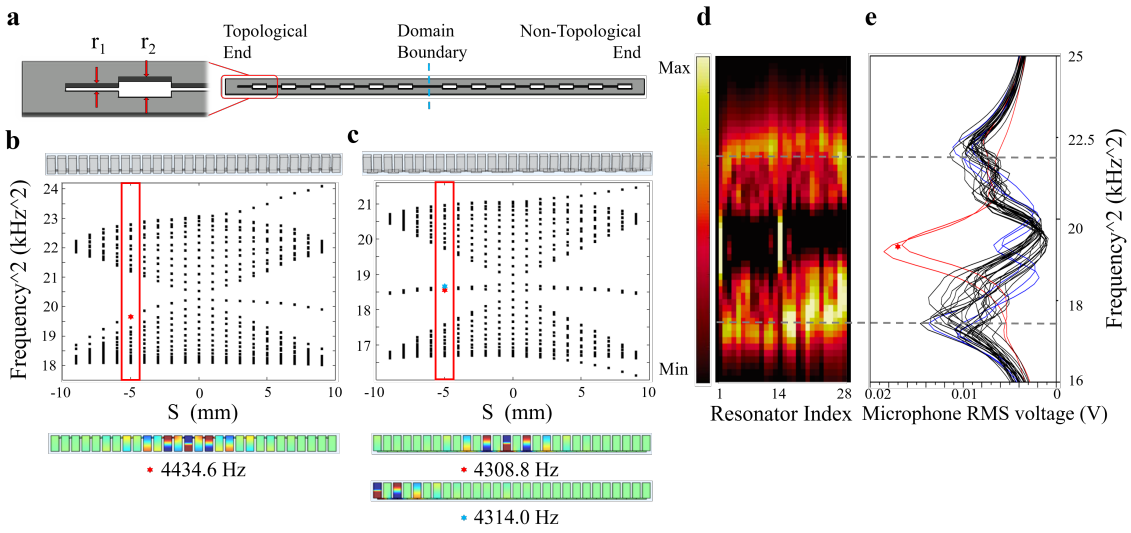

Figure 4.5 The SSH model consists of 28 resonators with a domain boundary in the middle, topologically non-trivial at one end and trivial at the other. **a.** Coupling bridges and its dimension. $r_1 = 5$ mm and $r_2 = 15$ mm. **b.** SSH model with side connection. The acoustic pressure field map below shows the interface mode at the red star in the spectrum when $S = -5$ mm. The model lacks edge modes. **c.** SSH model with bottom connection. Band structure and acoustic pressure field maps of both edge mode and interface mode. Blue and Red stars in the panel mark edge mode and interface mode, respectively. **d.** Experimentally measured local density of states, assembled from normalized microphone readings from the top of the block resonators. The bright dispersive modes indicates the bulk and edge modes. **e.** Collapse on the frequency axis of the intensity plot in **d**. The spectral gap can be clearly identified and the edge and interface modes show up in the gap marked with a red star.

via National Instruments USB-6122 data acquisition box and the data was stored for graphic renderings.

4.4 Conclusion

In this chapter, we investigated acoustic coupling that preserve symmetries through Comsol simulations and experiments. We tested couplings through the bottom, and with bridges at different height through the side. The first test was done on dimmers, then on single SSH set up, as well as one with interface. We observed that the simplest way for such coupling is to connect the resonators through the bottom. Coupling through the side requires a second connection. The advantages of coupling through the bottom is the modular structure of the set up. The resonators and coupling are printed individually, allowing for an easy variation in the coupling strength when the experiment requires. This platform has an exceptional flexibility since the resonators can be stored for further use.

CHAPTER 5

REVEALING TOPOLOGY IN METALS USING EXPERIMENTAL PROTOCOLS INSPIRED BY K-THEORY

This work has been published in Nature Communications. [Cheng et al., 2023]

Topological metals are conducting materials with gapless band structures and nontrivial edge-localized resonances. Their discovery has proven elusive because traditional topological classification methods require band gaps to define topological robustness. Inspired by recent theoretical developments that leverage techniques from the field of C^*-algebras to identify topological metals, here, we directly observe topological phenomena in gapless acoustic crystals and realize a general experimental technique to demonstrate their topology. Specifically, we not only observe robust boundary-localized states in a topological acoustic metal, but also re-interpret a composite operator—mathematically derived from the K-theory of the problem—as a new Hamiltonian whose physical implementation allows us to directly observe a topological spectral flow and measure the topological invariants. Our observations and experimental protocols may offer insights for discovering topological behaviour across a wide array of artificial and natural materials that lack bulk band gaps.

5.1 Introduction

Over the past two decades, immense progress has been made in predicting and observing topological phases of matter and their associated boundary-localized states in insulators [Hasan and Kane, 2010b, Qi and Zhang, 2011b, Bansil et al., 2016, Chiu et al., 2016b, Ozawa et al., 2019b] and semi-metals [Wang et al., 2012, Liu et al., 2014, Wang et al., 2013, Weng et al., 2015, Lv et al., 2015, Lu et al., 2015, Xiao et al., 2015, Li et al., 2018, Xie et al., 2019, Yang et al., 2019, Burkov et al., 2011, Xu et al., 2015, Fu et al., 2019]. These developments have been predicated upon the spectral isolation of the topological phenomena in these classes of systems; although materials such as Dirac semimetals [Wang et al.,

2012, Liu et al., 2014, Wang et al., 2013], Weyl semimetals [Weng et al., 2015, Lv et al., 2015, Lu et al., 2015, Xiao et al., 2015, Li et al., 2018, Xie et al., 2019, Yang et al., 2019], and nodal line/ring semimetals [Burkov et al., 2011, Xu et al., 2015, Fu et al., 2019] generally do not possess complete gaps in their band structures, the topological phenomena that manifest in these systems nevertheless appear within incomplete band gaps, allowing their boundary-localized states to be uniquely identified at some energy and quasimomentum. In contrast, the lack of band gaps (or, more generally, mobility gaps) in metals and other types of gapless systems has made their topological analysis extremely challenging and presently there are concentrated efforts in this direction [Chiu et al., 2016b]. While previous works have studied the bulk properties of topological metals, such as their topological responses and their relation to the geometry and topology of the Fermi surface [Hořava, 2005, Alexandradinata et al., 2018, Sun et al., 2020, Yuan and Fu, 2021, Kane, 2022], the focus of our work is on topological bulk-boundary correspondence in metals. As such, for the purposes of this study, we are using 'topological metal' to specifically refer to systems that exhibit a bulk-boundary correspondence that can be predicted using an invariant determined in the system's bulk, but whose topologically protected boundary-localized states or resonances are always degenerate in both energy and wave vector with bulk states. (In contrast, topological states in insulators and semimetals exhibit a range of energies and wave vectors where no bulk states exist.) From a theoretical perspective, the absence of spectral or dynamical gaps essentially precludes the use of topological band theory to identify the invariants of these systems, and prohibits such theories from predicting a measure of topological protection. Moreover, any boundary-localized phenomena in gapless systems will generally hybridize with the degenerate bulk states to create boundary-localized resonances, which complicates their experimental observation. Thus, despite the enormous advances that have been made in topological materials, the study of topological metals has remained almost entirely unexplored.

Recently, a general theoretical method for evaluating the topology of metallic and gapless systems was put forward, opening new opportunities for discovering topology in this class of systems that could not be previously explored [Cerjan and Loring, 2022]. This theoretical framework is rooted in the system's spectral localizer, which makes use of the system's real-space description and yields local invariants (synonymous with local markers) that are protected by local gaps [Loring, 2015, Loring and Schulz-Baldes, 2020, Loring and Schulz-Baldes, 2017]. The key concept that links traditional band theoretic approaches to this local understanding of a system's topology stems from a dual description of atomic limits, i.e., the limit where a complete basis of spatially localized Wannier functions exists. In band theoretic approaches, a group of bands is topologically trivial if they can be continued to an atomic limit without closing the band gap or breaking a symmetry; any obstruction to this continuation manifests as a non-trivial invariant [Kruthoff et al., 2017, Bradlyn et al., 2017, Po et al., 2017, Cano et al., 2018]. From a real-space operator perspective, an atomic limit's complete set of Wannier functions each have both a well-defined position and energy (in crystals they can be expressed as a flat band [Kitaev, 2009]). Thus, a d-dimensional atomic limit's Hamiltonian, $H^{(\mathrm{AL})}$, commutes with its position operators, $X_j^{(\mathrm{AL})}$, $[H^{(\mathrm{AL})}, X_j^{(\mathrm{AL})}] = 0$, for all $j \in 1, \ldots, d$. Using this mathematical observation, the spectral localizer ascertains a system's topology by determining whether there is an obstruction in continuing its H and X_j to be commuting (given similar restrictions as before), an analysis that can be performed using recent developments from the study of C^*-algebras [Loring, 2015, Hastings and Loring, 2011a]; any obstruction to continuing the system to possess commuting matrices yields a non-trivial invariant.

If a system's topology is instead linked to its multiple inequivalent atomic limits (e.g. as is common in systems with chiral- or crystalline-based topology), a system is only considered trivial if it can be continued to a chosen trivial atomic limit. Such cases are automatically handled by the spectral localizer, where it is necessary to explicitly specify the system's boundary and the grading operator that defines the chiral or crystalline symmetry to

evaluate the possibility of continuation. This pair of choices effectively fixes which atomic limit is considered to be trivial, and the spectral localizer ascertains whether there is an obstruction to continuing a given system to this trivial atomic limit. Altogether, by recasting the determination of a system's topology to real space, and not relying upon a bulk band gap to be the measure of topological protection, the spectral localizer is equally applicable to insulators and metals—meaningful local gaps that protect non-trivial topology can be found in both cases [Cerjan and Loring, 2022]. However, despite the prediction that the local topological invariants of gapless systems can be robust against system perturbations, robust topological metals that possess a bulk-boundary correspondence have not been previously identified in any platform.

Here, we theoretically develop and experimentally realize robust boundary-localized states protected by a bulk topological invariant in a gapless acoustic crystal. Unlike the forms of topology that can be found in semi-metals, the topological states we observe are degenerate with bulk states in both energy and wave vector. Our design is based on coupling a topologically gapped acoustic crystal to a gapless one, yielding a system that full-wave simulations show possesses a gapless resonant spectrum. Nevertheless, when domain boundaries are introduced, both simulations and experimental observations reveal that this two-layer system possesses boundary- and domain-localized states, and the topological origins of these states can be proven using the spectral localizer. To confirm the topological origin of these localized states, we develop an experimental protocol that treats the system's spectral localizer as the Hamiltonian of a related system, enabling the direct observation of the underlying system's spatially resolved K-theory, i.e., its local topology. Taken together, these measurements demonstrate that we have realized a topological metal. Given the generality of our experimental methodologies, these findings open opportunities to discover gapless topological phenomena across a broad range of natural and artificial materials.

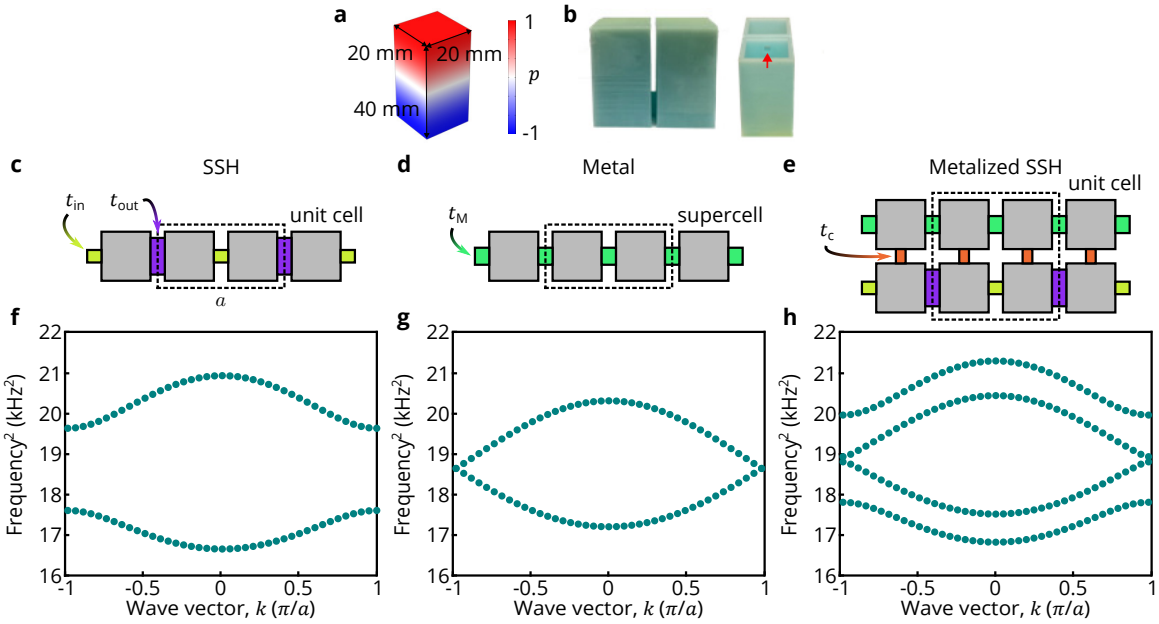

Figure 5.1 Designing a phononic topological metal. **a.** Simulated acoustic eigen-pressure field p for a single acoustic block resonator at the first elementary resonance mode with its geometry parameters, 20 mm by 20 mm by 40 mm. p is shown in normalized units. **b.** 3D-printed acoustic dimer consisting of one resonator belonging to the SSH layer and one resonator belonging to the metal layer, with the pair connected by an acoustic 3D printed bridge (red arrow points to one entrance to this bridge). The coupling bridge, parameterized by t_c, has width 3 mm, height 3 mm, and length 6 mm. **c,d,e,f,g,h** Schematics (**c,d,e**) and full wave simulations of the band structure (**f,g,h**) of the acoustic SSH lattice (**c,f**), acoustic metal lattice (**d,g**), and acoustic metallized SSH lattice (**e,h**). Band structures are shown in units of frequency squared to emphasize the symmetric spectrum due to chiral symmetry. The wave vector k lies in the first Brillouin Zone, which ranges from $-\pi/a$ to π/a, where $a = 52$ mm is the lattice constant. The couplings in the SSH lattice t_{in} and t_{out} are defined by channels with widths 15 mm (t_{in}) and 5 mm (t_{out}), and the same height 3 mm, and length 6 mm. The metal layer's coupling t_M stems from a channel with dimensions width 7 mm, height 3 mm, and length 6 mm.

5.2 Results and Discussion

5.2.1 Gapless topological phononic crystal

To realize our proof-of-principle topological metal, we use a phononic crystal, as this platform has been proven to be straightforward to fabricate and reconfigure (see Figure 5.1**a,b**) [Xiao et al., 2015, Li et al., 2018, Serra-Garcia et al., 2018, Xie et al., 2019, Yang et al., 2019, Ni et al., 2019c, Ni et al., 2019b, Wen et al., 2019, Xue et al., 2019a, Xue et al., 2019b, Apigo et al., 2019b, Peri et al., 2020, Cheng et al., 2020b, Ni et al., 2020, Chen et al., 2021, Xue et al., 2021, Jiang et al., 2021, Deng et al., 2022]. Heuristically, our aim for demonstrating such a phononic topological metal is to start with a topological insulator, couple it to a second lattice such that the combined system is gapless, and then probe it to observe boundary-localized states. For our specific design, we take the initial topological insulator to be a Su–Schrieffer–Heeger (SSH) lattice [Su et al., 1979], whose gapped spectrum is shown in Figure 5.1**c**. The second lattice is chosen to be a 1D monatomic lattice with uniform couplings, whose gapless spectrum is shown in Figure 5.1**d**. Here, we are enforcing the resonator geometry and spacing to be the same for both lattices and we are displaying the monatomic lattice's band structure as folded in to the same Brillouin zone as that of the SSH lattice. Finally, the two lattice layers are uniformly coupled together, resulting in a system with four resonators per unit cell that full-wave simulations show to exhibit a gapless spectrum, see Figure 5.1**e**. We refer to this two-layer lattice as an acoustic metallized SSH lattice. Note that the choice of lattice layer couplings (and identical resonator geometry) ensures that the full system respects chiral symmetry, which is necessary to allow for the possibility of topological states at mid-spectrum that are associated with this local symmetry classification. (As our 1D lattice has real coupling coefficients, it is in class BDI of the Altland–Zirnbauer symmetry classification, which possesses an integer invariant in 1D [Schnyder et al., 2008, Kitaev, 2009, Ryu et al., 2010].)

Our phononic crystals consist of acoustic cavities coupled together via grooved channels in the system's base and also via direct bridges (see Figure 5.1**a,b**). The geometry

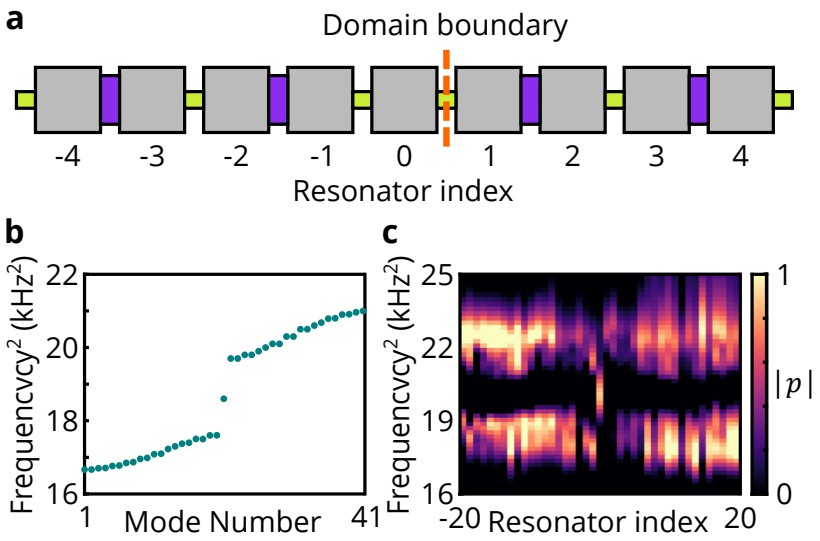

Figure 5.2 Observation of a phononic SSH lattice with a domain wall. **a.** Schematic of the domain wall in the phononic SSH lattice. Both edges of the lattice have topologically trivial terminations. **b.** Full wave simulations of the system's eigenfrequencies with 41 lattice sites in total. **c.** Measured local density of states (LDOS), assembled from microphone readings on 41 resonators of the acoustic SSH system. The observed pressure amplitude $|p|$ is shown in normalized units. A bulk band gap can be identified and the resonant mode in the bulk band gap is the domain boundary mode.

of the cavities is designed so that their fundamental axial pressure modes are well-separated in frequency from the rest of the resonant spectrum. The coupling strength between adjacent resonators is controlled through the width of the channels. The base of the system is laser-cut, while the dimmers of bridged resonating cavities are fabricated by 3D printing UV-curing resin. In particular, a bipartite single-layer metamaterial consisting of identical resonators and alternating coupling channel groove widths yields an accurate acoustic realization of the SSH lattice [Su et al., 1979] (see Supplementary Note 1). By designing a metamaterial with a domain boundary between two topologically distinct SSH insulating phases (without the added monatomic layer), and trivial outer edges, both simulation and experimental observations confirm that the system possesses a single topological resonant mode localized at the domain boundary, whose frequency is in the middle of the system's bulk band gap (see Figure 5.2). In addition, this topological mode's mid-gap frequency serves as implicit confirmation that the experimental platform can accurately reproduce chiral symmetry. To facilitate identification of the effects of chiral symmetry in our data we

show squared frequencies, as these are the eigenvalues of the acoustic wave equation that are equivalent to energy in the Schrödinger equation.

The phononic topological metal is experimentally realized by adding a layer of identical acoustic resonators, with uniform intra-layer coupling strength t_{M}, to the SSH layer and coupling the two layers together via uniform nearest-neighbor couplings t_{c}, see Figure 5.3**a,b,c**. In doing so, we are preserving the domain-wall boundary in the SSH layer and its trivial edge terminations, but there is no alteration to the monatomic layer at the domain boundary. Even so, this still yields a domain-wall in the combined system. Despite the full system's gapless spectrum, both full-wave numerical simulations (Figure 5.3**d**) and experimental observations (Figs. 5.3**e,f**) show that this metamaterial possesses edge- and domain wall-localized resonant states, whose appearance is linked to the relative strength of the coupling coefficients. In particular, this system exhibits four boundary-localized states in total, two that are approximately localized at the system's domain wall, and one at each edge, see Figure 5.3**f,g**. Moreover, we note that the phononic topological metal has many more topological states than one might initially expect—by itself, the SSH layer has topologically trivial edges (there are no edge-termination-localized states in Figure 5.2**c**) and a single domain-wall-localized state.

However, it is not possible to use topological band theories to predict the appearance of the four boundary-localized states seen in Figure 5.3**f,g**. Attempts to define a winding number (or another similar integer invariant for 1D chiral-symmetric systems) based on this crystal's bulk structure cannot work; the lack of a bulk band gap would require a path of matrix determinants that tried to characterize this winding to intersect the origin, making the winding number undefined [Asbóth et al., 2016]. On top of that, the topology of the observed boundary-localized resonances in the finite system cannot be understood from the presence of low-dimensional degeneracies in the periodic gapless system's spectrum, as is the case for topological semimetals. For a d-dimensional semimetal, its topology is connected to features in its band structure with dimension $\leq d-2$, and results in states

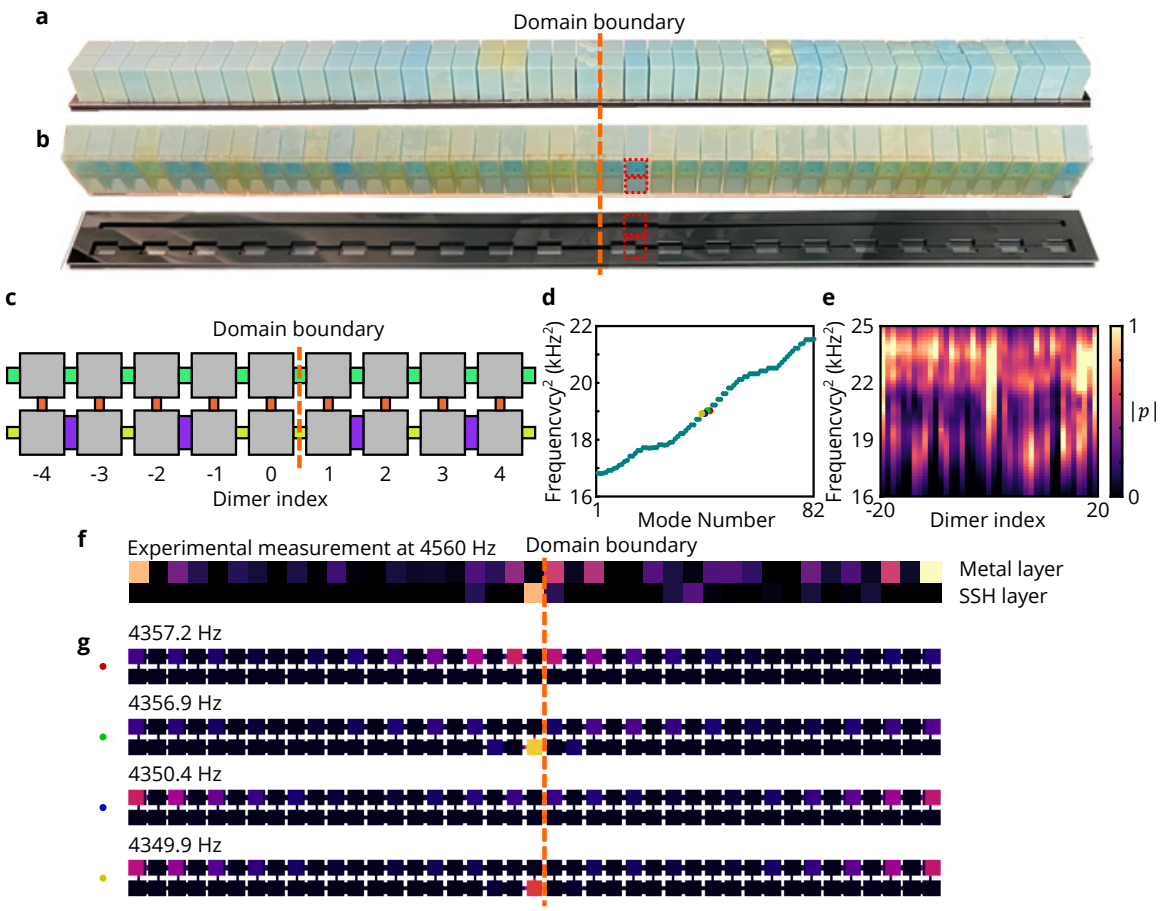

Figure 5.3 Experimental demonstration of phononic topological metal. **a.** Photograph of the fully assembled acoustic metallized SSH lattice consisting of block resonators and coupling bridges. **b.** Photograph of the inner structure, with all coupling bridges visible. The 3D-printed resonators are open at the bottom and are coupled through the 3D printed bridges and grooves in the black base when assembled. The acoustic resonators are embedded in the transparent acrylic plate (top) that sits above the black base (bottom). The red dotted squares indicate how the acoustic resonator dimers are mounted on the black base. **c.** Schematic of the phononic metallized SSH lattice showing the domain wall. The SSH layer is terminated in the same manner as Figure 5.2. **d.** Full-wave eigenfrequencies of the metallized SSH system consist of 41 dimers. **e.** Measured local density of states, assembled from microphone readings on the 41 dimers of the metallized SSH system. The observed pressure amplitude $|p|$ is shown in normalized units. LDOS is resolved by the dimer index. The data from the SSH resonator and the data from the metal resonator with the same dimer index are summed together. **f.** Measured acoustic pressure field distribution at 4560 Hz for the domain boundary- and edge-localized modes. **g.** Simulated acoustic eigen pressure fields of the four domain boundary- and edge-localized states. The colored dots in this panel correspond to those marked in **c**. The color indicates the absolute acoustic pressure $|p|$, which is displayed in normalized units.

on its $(d-1)$-dimensional surfaces that can be identified within an incomplete band gap. In contrast, our 1D periodic phononic topological metal (Figure 5.1**e**) cannot possess such low-dimensional band features, and upon introducing an edge or domain wall completely lacks any such kind of incomplete band gap (Figure 5.3**c,d**). Likewise, as the observed boundary-localized states are at mid-spectrum, we seek a topological classification that predicts and protects this spectral location, which precludes crystalline invariants [Kruthoff et al., 2017].

Altogether, standard theories of topology are unable to distinguish between the two bulk phases in this system and identify whether these localized states are of topological origin, or provide a measure of topological protection.

5.2.2 Theory of the spectral localizer

Instead, to prove that the observed localized states are of topological origin and that their existence can be tied to a bulk-boundary correspondence, we use the spectral localizer as this approach can be applied to systems that lack a bulk band gap [Cerjan and Loring, 2022]. In general, a system's spectral localizer combines its Hamiltonian and position operators using a non-trivial Clifford representation. Nonetheless, as our acoustic metamaterial is a 1D chiral symmetric system in which all of the couplings are real (i.e., its effective Hamiltonian is real-symmetric), its spectral localizer can be written in a reduced form as (see Supplementary Note 2)

$$\tilde{L}_{(x,E)}(X,H) = \kappa(X - xI)\Pi + H - iE\Pi. \tag{5.1}$$

Here, the spectral localizer can be evaluated at any choice of parameters $x, E \in \mathbb{R}$ (inside or outside of the system's spatial and spectral extent), κ is a tuning parameter that also ensures that the terms have compatible units, Π is the system's chiral operator, $H\Pi = -\Pi H$, and I is the identity matrix. Although the spectral localizer is basis independent, if H is written

in a tight-binding basis, X is simply a diagonal matrix whose entries correspond to the coordinates of each lattice site.

The spectral localizer (of appropriate dimension) can be used to both construct the relevant local topological invariant for a system in any symmetry class, as well as define the associated local gap. For the two-layer phononic topological metal considered here (or any other 1D system in class BDI), its local invariant is given by [Loring, 2015],

$$\nu_{\mathrm{L}}(x) = \tfrac{1}{2}\mathrm{sig}\left(\tilde{L}_{(x,0)}(X,H)\right) \in \mathbb{Z}, \tag{5.2}$$

where sig is the signature of a matrix, i.e., its number of positive eigenvalues minus its number of negative ones. Note, $\nu_{\mathrm{L}}(x)$ is only defined for $E = 0$, which reflects the fact that chiral symmetry can only protect states at the middle of the system's spectrum. Similarly, the local gap $\mu_{(x,E)}$ is given by the smallest singular value of $\tilde{L}_{(x,E)}$,

$$\mu_{(x,E)}(X,H) = \sigma_{\min}(\tilde{L}_{(x,E)}(X,H)). \tag{5.3}$$

More generally, $\mu_{(x,E)}$ is used to define the Clifford pseudospectrum of (X,H) [Cerjan et al., 2023].

Together, $\nu_{\mathrm{L}}(x)$ and $\mu_{(x,0)}$ yield a complete picture of a system's topology. Rigorously, $\nu_{\mathrm{L}}(x)$ is ascertaining whether the matrices H and $X - xI$ can be continued to the chosen trivial atomic limit while preserving both operators' real-symmetric form and chiral symmetry, and without closing the associated local gap, i.e., $\mu_{(x,0)} > 0$ during the entire continuation process; if $\nu_{\mathrm{L}}(x) = 0$, such a continuation is possible. (Here, the limit that is considered trivial is specified by the choice of Π in Equation (5.1).) Futhermore, this picture of topology is entirely local, different choices of x can yield different invariants—for x sufficiently far outside of the system's spatial extent, one expects to see a system with trivial

local topology, while x in the bulk of the system may reveal non-trivial local topology. At the domain boundary between these two regions, x_0, where $\nu_{\mathrm{L}}(x_0)$ changes, the local gap must close $\mu_{(x_0,0)} = 0$, which is a direct manifestation of bulk-boundary correspondence [Hastings and Loring, 2011a] and is an indication that there are eigenstates or resonances of H near x_0 at $E = 0$ [Cerjan et al., 2023].

When the Hamiltonian itself displays a global spectral gap, the topological invariant supplied by the spectral localizer coincides with the traditional 1D winding number [Asbóth et al., 2016] (or, more generally, even/odd Chern numbers or $\mathbb{Z}_2$ invariants, depending on the dimensionality and symmetry of the system [Loring and Schulz-Baldes, 2020, Loring and Schulz-Baldes, 2017]). In the absence of such a gap, $\nu_{\mathrm{L}}(x)$ has no analogue in the traditional way of applying K-theory: The spectral localizer simply pushes the applicability of the K-theoretic methods to previously unclassifiable systems and, in the present context, provides the means to formulate a bulk-boundary correspondence principle involving interface resonances as opposed to infinitely lived bound states. By a mechanism somewhat similar to one in complex scaling [Simon, 1978], the spectral localizer pushes away the continuum spectrum of H by opening a gap at locations away from the position being probed x, allowing for the study of spectral flows and their associated topology.

Applying the spectral localizer to a tight-binding approximation of the acoustic metallized SSH model proves that the localized states observed in this lattice are connected to a bulk topological invariant (see Supplementary Note 6). In particular, we numerically observe the local invariant $\nu_{\mathrm{L}}(x)$ in this system to change a few times, both at the system's boundaries and twice at the domain wall within the lattice's interior. Moreover, despite the fact that this lattice does not possess a bulk band gap, for most values of x we find that the localizer $\tilde{L}_{(x,E)}(X, H)$ does have a reasonable spectral gap at $E = 0$ that protects the bulk topological invariant.

5.2.3 Using the localizer as a system Hamiltonian

Beyond numerically calculating the phononic topological metal's local invariant and associated strength of protection, the form of the spectral localizer at $E = 0$ also inspires an experimental approach to verify the system's topology directly. In particular, because the reduced spectral localizer Equation (5.1) is Hermitian at $E = 0$, it can be reinterpreted as a set of Hamiltonians itself, with

$$\tilde{H}_x \equiv \tilde{L}_{(x,0)}(X, H) = \kappa(X - xI)\Pi + H, \tag{5.4}$$

in which $\kappa(X - xI)\Pi$ is now an on-site potential with a sign that is sublattice-dependent (i.e., a modification of the central frequencies of each resonator), and the choice of x re-centers this potential at a different lattice site (or anywhere in between lattice sites). Thus, by simulating and observing the spectrum of $\tilde{H}_x$, we are directly measuring the spectrum of $\tilde{L}_{(x,0)}$, which, through Equations (5.2) and (5.3), determines the topology and associated protection of the underlying system described by H at x.

In practice, this reinterpretation presents a challenge, as $\|X - xI\|$ can become arbitrarily large as the lattice's size increases, but it is not possible to alter a resonator's geometry to yield arbitrarily large or small resonance frequencies. Instead, we can circumvent this challenge by using the substitution

$$\kappa(X - xI)\Pi \to \kappa \left[\tanh\left(\frac{X - xI}{\alpha}\right)\right]\Pi, \tag{5.5}$$

such that

$$\tilde{H}_x = \kappa \left[\tanh\left(\frac{X - xI}{\alpha}\right)\right]\Pi + H. \tag{5.6}$$

As this bounded operator is linear in the vicinity of $x = 0$ (the range of approximate linearity is set by α), one can prove that it preserves the necessary information for determining the system's topology using Equation (5.2) (see Supplementary Note 3). Additionally, this choice of alteration to the system's resonators can be experimentally realized for lattices of any size (see Figure 5.4).

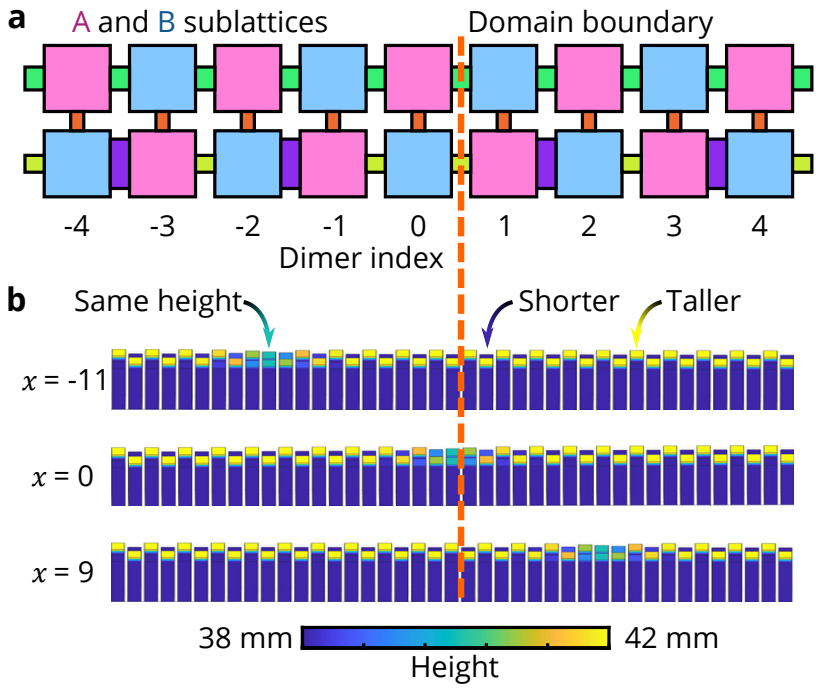

Figure 5.4 Experimental protocol for observing the spectral localizer. **a.** Schematic of the spectrally localized phononic metamaterial with the domain wall shown. The two sublattices of the system are indicated in magenta and cyan, which correspond to entries of $+1$ and -1 in Π, respectively. **b.** The configurations of the system when the localizer is centered at $x = -11$, $x = 0$, and $x = 9$. The height of each resonator above 38 mm is indicated by the color scale. As the underlying phononic topological metal in Figure 5.3 uses resonators that are 40 mm tall, and small changes to the resonator volume change its frequency without changing its couplings, this coloration is effectively showing the on-site potential added in Equation (5.6).

We directly confirm the topological behavior of the phononic topological metal described by the Hamiltonian H by numerically and experimentally observing the properties of its spectrally localized counterpart given by $\tilde{H}_x$ at many different choices of x (a realization for a single x is shown in Figure 5.5**a**). In particular, the sublattice-dependent on-site potential is realized by modifying all of the resonator heights by up to 2 mm, which preserves their well-separated fundamental axial mode but yields a shift their frequency (i.e.,

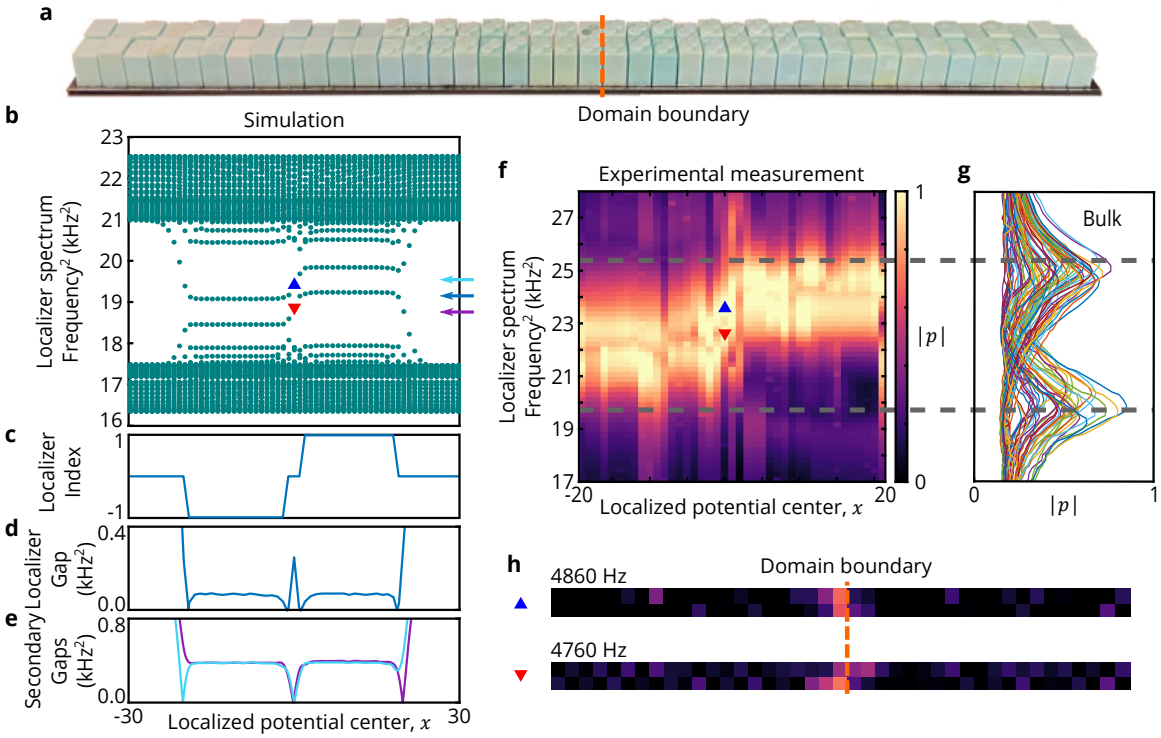

Figure 5.5 Observation of topology using a spectrally localized acoustic metamaterial. **a.** Photograph of the fully assembled spectrally localized metamaterial with the added sublattice-dependent on-site energies to the underlying metallized SSH lattice. The resonators that comprise this system can be re-assembled to realize different choices of the center of the localized potential x in Equation (5.6). **b.** COMSOL simulated resonant spectrum of the spectrally localized metamaterial as the position of the localized potential's center x is varied, demonstrating the existence of the two bands in the dynamical localization gap. **c,d,e** Localizer index (**c**), localizer gap (**d**), and secondary gaps (**e**) derived from the full-wave simulated spectrum. The localizer index and gap are calculated using the mid-spectrum frequency indicated in **b** (blue arrow on right), and the two frequencies chosen for calculating the secondary gaps are similarly indicated (cyan and magenta arrows on right). **f.** Experimental mapping of the local density of states as the localized potential's center is moved (constructed from microphone readings on the dimer where the localized potential is centered x), confirming the existence of the two central eigenvalues for varying x seen in **b**. $\alpha = 2.5a$ and $\kappa = 1.85$ kHz^2 in Equation (5.6) were used in our simulations and experiments, where a is the lattice constant. The observed pressure amplitude $|p|$ is shown in normalized units. **g.** Measured pressure in normalized units for the spectrally localized system's bulk eigenvalues constructed from the microphone readings on the bulk resonators at least three resonators away from the localized potential center. The gray lines in **f** and **g** are showing that the spectrally localized system's two central sets of eigenvalues are well separated from the system's remaining eigenvalues. **h.** Experimentally measured mode profiles at 4760 Hz and 4860 Hz when $x = 0$ using the same color map as **f**. The red and blue triangles in **b** and **f** correspond to the frequency and localized potential center chosen for observing these data.

a different on-site potential). First, full-wave simulations of the localized metamaterial, $\tilde{H}_x$, demonstrate that there are four x locations in the underlying system where the local invariant changes and the local gap closes (Figure 5.5**b,c,d**), two locations at the outer edges of the system, and two next to the domain boundary. As locations where $\mu_{(x,0)} = 0$ predict the presence of states of H, the localized states seen in the original phononic topological metal (Figure 5.3**f,g**) are a direct manifestation of bulk-boundary correspondence and are necessarily of topological origin. Thus, despite the absence of a bulk band gap in the system, these topological states are protected by the non-zero local gap $\mu_{(x,0)} \approx 0.1$ kHz^2 surrounding the locations where these states appear. In other words, chiral-preserving perturbations to the system $H \to H + \delta H$ cannot alter the local topology at x so long as $\|\delta H\| < \mu_{(x,0)}$. Furthermore, we note that these states possess additional protection due to a relatively large secondary gap ≈ 0.4 kHz^2, see and Figure 5.5**e** and Supplementary Note 4. Heuristically, every gap in the localizer can be associated with an element in a K-theory group, and thus can provide some form of topological protection [Schulz-Baldes and Stoiber, 2021]. Although most such gaps are too small for the resulting topology to be physically robust, for this particular system the secondary gap is relatively large and thus provides strong protection for one of the two states at the domain boundary at the system's center.

We also experimentally realize the localized metamaterial, and directly characterize the changes in the underlying system's local K-theory (Figure 5.5**f,g,h**). In particular, the simulated resonance spectrum is reproduced with high fidelity by experimental measurements, confirming the topological properties of our phononic topological metal. Likewise, the two central bands (Figure 5.5**f**) are observed to be well separated from the remainder of the spectrally localized system's bulk bands (Figure 5.5**g**). Although different choices of x in $\tilde{H}_x$ yield distinct physical systems (see Figure 5.4**b**), our acoustic metamaterial is re-configurable, and thus we do not need to fabricate a new system for each choice of x shown in Figure 5.5. The discrepancies between simulation and experiment are

likely the result of fabrication imperfections and variations, as well as measurement errors. However, the discrepancy observed in Figure 5.5 is still of a similar magnitude to those observed both Figs. 5.2 and 5.3. In particular, the observed discrepancy in the SSH lattice (Figure 5.2) shows that these differences are standard to the acoustic metamaterial platform, and are not substantially larger or smaller for our metallic (Figure 5.3) or spectrally localized systems (Figure 5.5).

Thus, altogether, our experimental results, coupled with our full-wave simulations, prove that our underlying phononic metamaterial (Figure 5.3) is a gapless topological material.

5.2.4 The underlying K-theory

The relative simplicity of the equations of the spectral localizer and the local topological invariants it provides tends to obscure the K-theory that it rests on. Thus, to show how our experimental protocol for altering a system to directly observe its topology stems from K-theory, we provide a brief discussion for an interested reader aimed at illuminating the spectral localizer's mathematical foundation.

A traditional form of K-theory, topological K-theory [Atiyah, 1967, Karoubi, 2008], works with continuous functions that map from a given topological space to a space of structured matrices. These spaces of structured matrices are called classifying spaces, as they can be used to compute all 10 K-theory groups associated to the original given space. (Classifying spaces for classes of real or complex vector bundles would be special cases associated with this mapping.) A newer, more powerful form of K-theory is the K-theory of C^*-algebras [Blackadar, 1986], which still applies when one has momentum space but also applies when momentum space is lost. Here, we work with modified forms of C^*-algebra K-theory [Boersema and Loring, 2016, Hastings and Loring, 2011b, Loring, 2015, Trout, 2000, Browne, 2019, Doll and Schulz-Baldes, 2021, Großmann and Schulz-Baldes, 2016] that are more directly applicable to finite systems. Moreover, these newer forms of K-theory

lead to efficient numerical algorithms and are adaptable to different symmetry classes. The main speedup of these approaches comes from avoiding spectral flattening, as numerically, operations like projecting into an occupied subspace tend to produce dense matrices even when the original system can be described with sparse matrices.

Following Ref. [Kitaev, 2009], we briefly review how classical topological K-theory arises in the case of a periodic 1D system in class BDI. The position operator is used to define momentum space, which is a copy of the circle $\mathbb{T}^1$. The chirality of the Hamiltonian means

$$H(k) = \begin{bmatrix} 0 & U(k) \\ U^\dagger(k) & 0 \end{bmatrix}. \tag{5.7}$$

If we have taken the optional step of spectrally flattening H, we find that $U(k)$ is unitary. Thus, the topology in class BDI arises from attempting to classify the ways in which continuous functions can map from the circle to the classical groups of unitary matrices; that is, homotopy classes of elements of $C(\mathbb{T}^1, \mathcal{U}(n))$. Time-reversal symmetry manifests itself as $U^*(k) = U(-k)$. As Kitaev explains [Kitaev, 2009], homotopy classes in $C(\mathbb{T}^1, \mathcal{U}(n))$ can be used to form a group, one of the classic groups in topological K-theory [Karoubi, 2008]. Finally, the K-theory group element determined by $H(k)$ can be calculated using a winding number.

For non-periodic, finite 1D systems in class BDI, we use the form of K-theory that associates groups to certain algebras. The relevant algebra is $\mathcal{A} = \boldsymbol{M}_{2n}(\mathbb{C})$, treated as a graded, real C^*-algebra, and $2n$ is the number of sites in the system. The grading is determined by Π and we use the standard reality structure (real matrix means real entries). The zeroth group of K-theory for this algebra $K_0(\mathcal{A})$ is built out of out of homotopy classes of $2n$-by-$2n$ unitary matrices U that also satisfy $\Pi U \Pi = U^\dagger$ and $U^\top = U$ [Trout, 2000]. Nonetheless, if we want to avoid spectral flattening, we can instead look at homotopy classes

of invertible matrices M such that $\Pi M \Pi = M^\dagger$ and $M^\top = M$. Finally, the element of $K_0(\mathcal{A})$ determined by M is calculated using half the signature of $M\Pi$.

To apply this general discussion to the spectral localizer, consider the full 1D spectral localizer at $E = 0$

$$L_{(x,0)}(X, H) = \begin{bmatrix} 0 & \kappa(X - xI) - iH \\ \kappa(X - xI) + iH & 0 \end{bmatrix}, \tag{5.8}$$

which at most positions x will contain two invertible matrices, $M_x = \kappa(X - xI) + iH$ and its adjoint. Notice that $M_x\Pi$ is Hermitian (but not real), and thus we can determine the underling physical system's topology by calculating $\text{sig}(M_x\Pi)$. In [Loring, 2015] it was established that in the BDI symmetry class $M_x\Pi$ is unitarily equivalent to the real symmetric matrix $\kappa(X - xI)\Pi + H$ (i.e., Equation (5.4)), and thus $\text{sig}(M_x\Pi) = \text{sig}\left(\tilde{H}_x\right)$, which is what is used in Equation (5.2).

Altogether, a more standard approach to topological materials would consider the unitary U_x that is derived from M_x by spectral flattening (that is, U_x is the unitary polar factor of M_x). Then one can apply the graded trace, which is more familiar in pure math than the graded signature. However, since

$$\text{tr}\left(U_x\Pi\right) = \text{sig}\left(M_x\Pi\right) = \text{sig}\left(\tilde{H}_x\right) \tag{5.9}$$

we have many mathematically equivalent formulas to choose from to determine the underlying system's topology. In particular, the latter two of these formula can be immediately recognized from the invertible matrix form of C^*-algebra K-theory that underpin the spectral localizer. From the perspective of numerical efficiency, the formula involving U_x would be the slowest, assuming one actually performs the spectral flattening.

The formula involving $\tilde{H}_x$ will be the fastest, as this matrix will be real, symmetric, and (usually) sparse.

Thus, as $\tilde{H}_x$ is the Hamiltonian for the localized system (Figure 5.5) that we realize to observe the topology of the underlying phononic topological metal (Figure 5.3), our experimentally methodology is inextricably linked to the K-theory of C^*-algebras.

5.3 Methods

5.3.1 Fabrication

Our fabrication process is modular and the acoustic crystals are assembled from parts that are independently manufactured with different automated process. This approach enables a high throughput of acoustic crystals, which can be disassembled and stored after use.

One leg of the process is the manufacturing of the supporting bases, which consist of two layers of 3-mm thick black acrylic plates (Figure 5.3**b**) and one top layer of 1.5-mm thick transparent acrylic plates (Figure 5.3**a,b**), of which the top transparent layer and middle black layer have through holes, laser-cut at specific geometries with the Boss Laser-1630 Laser Engraver. The middle layer with 3mm deep through channels provides coupling channels between the dimers. The top transparent layer with through square holes holds the dimers in place.

The resonators were manufactured using an Anycubic Photon 3D printer, which uses UV resin and has $47\ \mu m$ XY-resolution and $10\ \mu m$ Z-resolution. The thickness of their walls is 2 mm, to ensure a good quality factor and to justify rigid boundaries in our numerical simulations. The inner dimensions of the resonators are supplied in Figure 5.1**a,b**. For the metallized-SSH system, the resonators are 3D printed as dimers with identical narrow channels connecting the resonators. To implement the spectral localizer, the resonators were printed with different heights according to the algorithm Equation (5.6) and were made ready for the assembling.

The resonators were mounted and coupled through the channels grooved in the acrylic plates of the base. Let us specify that the resonators are interchangeable so that they can be move around and acoustic crystals with different probe positions can be generated, as described in the main text. Finally, we note that although the coloration of the resonators is not uniform in either of the structures shown in Figure 5.3**a,b** or 5.5**a**, this is simply an artifact of the fabrication process, and these color differences do not impact their behavior in any way.

5.3.2 Experimental protocols

The protocol for the acoustic measurements reported in Figure 5.3 and Figure 5.5 was as follows: Sinusoidal signals of duration 1 s and amplitude of 0.5 V were produced with a Rigol DG 1022 function generator and applied on a speaker placed in a porthole opened in a resonator. A dbx RTA-M Reference Microphone with a Phantom Power was inserted in a porthole opened in the same resonator where the speaker was inserted and acquired the acoustic signals. The signals were read by a custom LabVIEW code via National Instruments USB-6122 data acquisition box and the data was stored on a computer for graphic renderings.

The local densities of states reported in Figure 5.3**d** and Figure 5.5**f,g** were obtained by integrating the local density of states acquired from resonators whose index are the same as the position of the probe. Same instrumentation was used. The measurements were repeated with moving the position of the probe. For each measurement, the frequency was scanned from 4200 Hz to 5200 Hz in 10 Hz steps.

5.3.3 Simulation

The simulations reported in Figs. 5.1, 5.2, 5.3, and 5.5 were performed with the COMSOL Multiphysics pressure acoustic module. The wave propagation domains shown in Figure 5.1 were filled with air with a mass density 1.3 kg/m^3 and the sound's speed was fixed at 343

m/s, appropriate for room temperature. Because of the huge acoustic impedance mismatch compared with air, the 3D printing UV resin material was considered as hard boundary.

5.4 Conclusion

In conclusion, we have demonstrated a topological metal in an acoustic metamaterial and directly observed its boundary-localized states despite its lack of a bulk band gap. To do so, we have used the spectral localizer, a local theory of topological materials that is able to predict topological phenomena, and a measure of topological protection, even in the absence of a bulk band gap. In addition, we have introduced an experimental protocol that uses a system's spectral localizer as its Hamiltonian, providing a direct probe of the underlying system's local K-theory. Here, it is worth emphasizing that this protocol can be applied to any topological system. Although our specific demonstration has leveraged the system's symmetries to yield a real-symmetric spectral localizer, the spectral localizer for any system is, by definition, Hermitian, and as such, it can always be adapted to be an observable system. Thus, the overall methodology that we have introduced may enable the prediction and observation of topological metals across a broad array of systems, including materials that exhibit higher-order topology and those whose topology is determined by its crystalline symmetries. Finally, as the spectral localizer takes an operator-based, rather than eigenstate-based, approach to topology, it is potentially broadly applicable to interacting systems, a class of systems that traditional band theories of topology have had difficulty gaining traction with.

CHAPTER 6

SUMMARY

In this dissertation, the role of topological phonons has been investigated in different length scales and their potential applications in various systems. The dissertation endeavors to enhance our comprehension of the significance and potential of topological phonons in diverse systems by exploring two aspects: the acoustic resonator properties of tubulin proteins in microtubules and the application of topological phonons in the context of acoustic metamaterials.

In Chapter 2, we established that microtubules are predicted to exhibit characteristics of naturally occurring topological phononic crystals, with the localization of vibrational energy playing a crucial role in dynamic instability. The future plan is to explore the excitation of higher vibrational modes of microtubules to gain a comprehensive understanding of the complete phonon spectrum. Up until the current stage of the research, the observed vibrations of microtubules were primarily induced by the thermal energy present in the surrounding water, limiting our ability to observe higher vibrational modes. To gain insights into the local mechanical properties of microtubules, including protein-protein force fields and the effects of various proteins and chemical compounds such as motor proteins and Taxol, the methods presented in this study can be further enhanced. Achieving fine-scale measurements necessitates the fabrication of an experimental platform capable of capturing microtubule movements with micron or even nanometer precision.

In Chapter 3, the initial version of our nanofluidic device was introduced, serving the purpose of isolating a single microtubule, and the next step will be incorporating electrodes into the nanofluidic device. This addition enables us to exert precise control over the vibrations of the isolated microtubule, unlocking new possibilities for mapping its phonon spectrum with enhanced precision and detail. With electrodes positioned along the sides of

the device, we gain the ability to selectively stimulate specific vibrational modes and delve into the diverse range of vibrational behaviors exhibited by the microtubule.By integrating electrodes into the nanofluidic device, we achieve a notable advancement that empowers us to manipulate and study the vibrational properties of the microtubule within a controlled environment. Figure 6.1 shows the microfluidic device that was constructed for experimental testing purposes. The device features seven pairs of electrodes positioned on each side of the microchannel. For a detailed depiction of the device layout, refer to Figure 1.3. The microchannel is intentionally designed to have a width of 1.5 microns in order to avoid the higher costs associated with using e-beam lithography. This decision allows for a more cost-effective fabrication process while we were learning how to deposit electrodes and refining our techniques in working with the electrodes. Given the net charge of tubulin protein, capacitance sensing could be employed to detect the movement of the microtubule relative to electrodes positioned along its length. Fabricating a nanofluidic device with electrodes is within reach, leveraging advancements in e-beam lithography, improved packing techniques for fluidic platforms, the device will enable us to selectively stimulate specific vibrational modes and delve into the comprehensive spectrum of vibrational behaviors exhibited by the microtubule. Through this innovative device, we can gain a deeper understanding of the intricate dynamics and properties of the microtubule with enhanced precision and control.

In Chapter 4, we investigated the application of topological phonons in the context of acoustic metamaterials. Acoustic metamaterials are engineered materials designed to control and manipulate sound waves. By exploring the potential of topological phonons in acoustic metamaterials, we proposed an experimental approach which offers a modular platform for coupling acoustic crystals, supporting topologically protected edge and interface states while preserving desired symmetry. Chapter 5 explores the application of the same coupling method to a topological acoustic metal system. Inspired by recent theoretical advancements, this study directly observes topological phenomena in gapless acoustic crystals and develops an experimental technique to demonstrate their

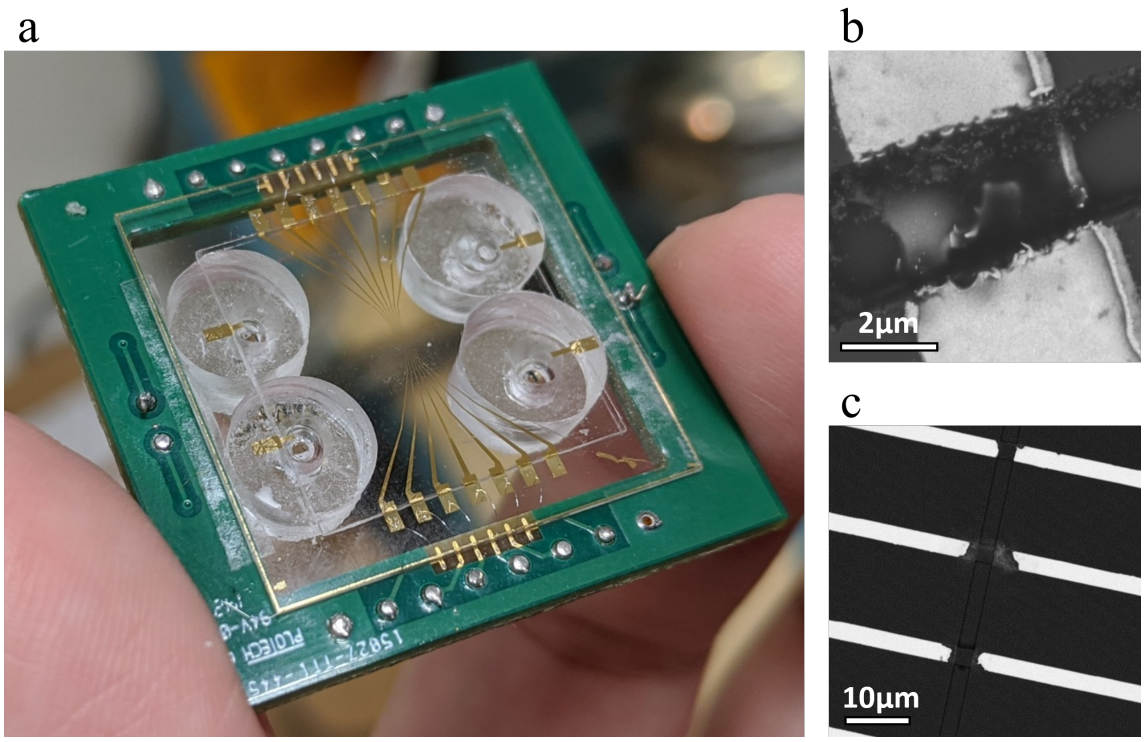

Figure 6.1 Microfluidic device with 7 pairs of electrodes. **a.** On a compact platform, a microfluidic device is implemented, where the electrodes are securely connected to pins on the platform through wire bonding. The device incorporates 4 PDMS reservoirs that are firmly attached to serve as inlet and outlet ports. **b.** The channel width of the device is approximately 1.5-2 microns, while the width of the electrodes ranges from 2 to 4 microns. It's important to note that the slight variation in the measurements is attributed to the inherent limitations of the lithography process. **c.** The electrodes are uniformly spaced at intervals of 20 microns.

topology. This technique allows for the observation of robust boundary-localized states, the reinterpretation of a composite operator as a new Hamiltonian, and the measurement of topological invariants.

Currently, our research primarily focuses on investigating the topological phonons in one-dimensional and two-dimensional topological acoustic systems. Nevertheless, the realization of higher-order topological metamaterials, which are more intricate yet intriguing, remains a significant challenge. The future plan will involve how to apply the bottom coupling method in three-dimensional topological acoustic system. The impact of our research extends to a wide range of applications, including noise control, information transfer, acoustic-based sensing and imaging, as well as quantum information processing. By introducing a novel approach for implementing and observing topological excitation modes solely based on material structures, our work opens up exciting possibilities in topological acoustics for manipulating and controlling sound in fundamentally innovative ways. We hope that our efforts will serve as inspiration for the design of even more captivating topological metamaterials, following the same principles. This emerging field draws inspiration from remarkable advancements in condensed matter physics, quantum mechanics, and mathematics, leveraging the unique properties of acoustic metamaterials to enable novel forms of sound transport. We anticipate that topological acoustics will pave the way for transformative advancements in sound control, with significant implications for both fundamental science and practical technologies.

REFERENCES

[Al Jahdali and Wu, 2016] Al Jahdali, R. and Wu, Y. (2016). High transmission acoustic focusing by impedance-matched acoustic meta-surfaces. *Applied Physics Letters*, 108(3):031902.

[Alexandradinata et al., 2018] Alexandradinata, A., Wang, C., Duan, W., and Glazman, L. (2018). Revealing the topology of Fermi-surface wave functions from magnetic quantum oscillations. *Physical Review X*, 8(1):011027.

[Apigo et al., 2019a] Apigo, D. J., Cheng, W., Dobiszewski, K. F., Prodan, E., and Prodan, C. (2019a). Observation of topological edge modes in a quasiperiodic acoustic waveguide. *Physical Review Letters*, 122(9):095501.

[Apigo et al., 2019b] Apigo, D. J., Cheng, W., Dobiszewski, K. F., Prodan, E., and Prodan, C. (2019b). Observation of topological edge modes in a quasiperiodic acoustic waveguide. *Physical Review Letter*, 122(9):095501.

[Asbóth et al., 2016] Asbóth, J. K., Oroszlány, L., and Pályi, A. (2016). A short course on topological insulators. *Lecture Notes in Physics*, 919:166.

[Aslam and Prodan, 2019] Aslam, A. A. and Prodan, C. (2019). Experimentally measured phonon spectrum of microtubules. *Journal of Physics D: Applied Physics*, 53(025401).

[Atiyah, 1967] Atiyah, M. F. (1967). *K-theory*. W. A. Benjamin, Inc., New York-Amsterdam. Lecture notes by D. W. Anderson.

[Bansil et al., 2016] Bansil, A., Lin, H., and Das, T. (2016). Colloquium: Topological band theory. *Reviews of Modern Physics*, 88(2):021004.

[Blackadar, 1986] Blackadar, B. (1986). *K-theory for operator algebras*, volume 5 of *Mathematical Sciences Research Institute Publications*. Springer-Verlag, New York.

[Boersema and Loring, 2016] Boersema, J. L. and Loring, T. A. (2016). K-theory for real C^*-algebras via unitary elements with symmetries. *New York Journal of Mathematics*, 22:1139–1220.

[Bradlyn et al., 2017] Bradlyn, B., Elcoro, L., Cano, J., Vergniory, M. G., Wang, Z., Felser, C., Aroyo, M. I., and Bernevig, B. A. (2017). Topological quantum chemistry. *Nature*, 547(7663):298–305.

[Browne, 2019] Browne, S. L. (2019). A Bott periodicity proof for real graded C^*-algebras. *Journal of Mathematical Analysis and Applications*, 479(1):658–672.

[Burkov et al., 2011] Burkov, A., Hook, M., and Balents, L. (2011). Topological nodal semimetals. *Physical Review B*, 84(23):235126.

[C. Iliescu, 2012] C. Iliescu, H. Taylor, M. A. J. M. S. F. (2012). A practical guide for the fabrication of microfluidic devices using glass and silicon. *Biomicrofluidics*, 6:016505.

[Cannon et al., 2004] Cannon, Donald M., J., Flachsbart, B. R., Shannon, M. A., Sweedler, J. V., and Bohn, P. W. (2004). Fabrication of single nanofluidic channels in poly(methylmethacrylate) films via focused-ion beam milling for use as molecular gates. *Applied Physics Letters*, 85(7):1241–1243.

[Cano et al., 2018] Cano, J., Bradlyn, B., Wang, Z., Elcoro, L., Vergniory, M. G., Felser, C., Aroyo, M. I., and Bernevig, B. A. (2018). Building blocks of topological quantum chemistry: Elementary band representations. *Physical Review B*, 97(3):035139.

[Cao et al., 2002] Cao, H., Tegenfeldt, J. O., Austin, R. H., and Chou, S. Y. (2002). Gradient nanostructures for interfacing microfluidics and nanofluidics. *Applied Physics Letters*, 81(16):3058–3060.

[Cerjan and Loring, 2022] Cerjan, A. and Loring, T. A. (2022). Local invariants identify topology in metals and gapless systems. *Physical Review B*, 106:064109.

[Cerjan et al., 2023] Cerjan, A., Loring, T. A., and Vides, F. (2023). Quadratic pseudospectrum for identifying localized states. *Journal of Mathematical Physics*, 64(2):023501.

[Chen et al., 2021] Chen, Z.-G., Zhang, R.-Y., Chan, C. T., and Ma, G. (2021). Classical non-Abelian braiding of acoustic modes. *Nature Physics*, pages 1–6.

[Cheng et al., 2023] Cheng, W., Cerjan, A., Chen, S., Prodan, E., Loring, T. A., and Prodan, C. (2023). evealing topology in metals using experimental protocols inspired by k-theory. *Nature Communications*, 14(3071):1–9.

[Cheng et al., 2020a] Cheng, W., Prodan, E., and Prodan, C. (2020a). Experimental demonstration of dynamic topological pumping across incommensurate bilayered acoustic metamaterials. *Physical Review Letters*, 125:224301.

[Cheng et al., 2020b] Cheng, W., Prodan, E., and Prodan, C. (2020b). Experimental demonstration of dynamic topological pumping across incommensurate bilayered acoustic metamaterials. *Physical Review Letter*, 125(22):224301.

[Chiu et al., 2016a] Chiu, C.-K., Teo, J. C. Y., Schnyder, A. P., and Ryu, S. (2016a). Classification of topological quantum matter with symmetries. *Reviews of Modern Physics*, 88:035005.

[Chiu et al., 2016b] Chiu, C.-K., Teo, J. C. Y., Schnyder, A. P., and Ryu, S. (2016b). Classification of topological quantum matter with symmetries. *Reviews of Modern Physics*, 88(3):035005.

[Coutant et al., 2021] Coutant, A., Sivadon, A., Zheng, L., Achilleos, V., Richoux, O., Theocharis, G., and Pagneux, V. (2021). Acoustic su-schrieffer-heeger lattice: Direct mapping of acoustic waveguides to the su-schrieffer-heeger model. *Physical Review B*, 103:224309.

[Deng et al., 2022] Deng, Y., Benalcazar, W. A., Chen, Z.-G., Oudich, M., Ma, G., and Jing, Y. (2022). Observation of degenerate zero-energy topological states at disclinations in an acoustic lattice. *Physical Review Letter*, 128(17):174301.

[Derry et al., 1997] Derry, W. B., Wilson, L., Khan, I. A., Ludueña, R. F., and Jordan, M. A. (1997). Taxol differentially modulates the dynamics of microtubules assembled from unfractionated and purified β-tubulin isotypes. *Biochemistry*, 36(12):3554–3562.

[Desai and Mitchison, 1997] Desai, A. and Mitchison, T. J. (1997). Microtubule polymerization dynamics. *Annual Review of Cell and Developmental Biology*, 13:83–117.

[Doll and Schulz-Baldes, 2021] Doll, N. and Schulz-Baldes, H. (2021). Skew localizer and z2-flows for real index pairings. *Advances in Mathematics*, 392:108038.

[Feizabadi and Rosario, 2017] Feizabadi, M. S. and Rosario, B. (2017). MCF7 microtubules: Cancer microtubules with relatively slow and stable dynamic in vitro. *Biochemical and Biophysical Research Communications*, 484(2):354–357.

[Fleury et al., 2016] Fleury, R., Khanikaev, A., and Alù, A. (2016). Floquet topological insulators for sound. *Nature Communications*, 7(11744).

[Fu et al., 2019] Fu, B.-B., Yi, C.-J., Zhang, T.-T., Caputo, M., Ma, J.-Z., Gao, X., Lv, B., Kong, L.-Y., Huang, Y.-B., Richard, P., et al. (2019). Dirac nodal surfaces and nodal lines in zrsis. *Science Advances*, 5(5):eaau6459.

[Fygenson et al., 1994] Fygenson, D. K., Braun, E., and Libchaber, A. (1994). Phase diagram of microtubules. *Physical Review E*, 50(2):1579–1588.

[Großmann and Schulz-Baldes, 2016] Großmann, J. and Schulz-Baldes, H. (2016). Index pairings in presence of symmetries with applications to topological insulators. *Communications in Mathematical Physics*, 343:477–513.

[Hasan and Kane, 2010a] Hasan, M. Z. and Kane, C. L. (2010a). Colloquium: Topological insulators. *Reviews of Modern Physics*, 82:3045–3067.

[Hasan and Kane, 2010b] Hasan, M. Z. and Kane, C. L. (2010b). Colloquium: Topological insulators. *Reviews of Modern Physics*, 82(4):3045–3067.

[Hastings and Loring, 2011a] Hastings, M. B. and Loring, T. A. (2011a). Topological insulators and C^*-algebras: Theory and numerical practice. *Annals of Physics*, 326(7):1699–1759.

[Hastings and Loring, 2011b] Hastings, M. B. and Loring, T. A. (2011b). Topological insulators and C^*-algebras: Theory and numerical practice. *Annals of Physics*, 326(7):1699–1759.

[Haubert et al., 2006] Haubert, K., Drier, T., and Beebe, D. (2006). Pdms bonding by means of a portable, low-cost corona system. *Lab on a Chip*, 6:1548–1549.

[Hawkins et al., 2010] Hawkins, T., Mirigian, M., Selcuk Yasar, M., and Ross, J. L. (2010). Mechanics of microtubules. *Journal of Biomechanics*, 43(1):23–30.

[Hawkins et al., 2012] Hawkins, T. L., Mirigian, M., Li, J., Yasar, M. S., Sackett, D. L., Sept, D., and Ross, J. L. (2012). Perturbations in microtubule mechanics from tubulin preparation. *Cellular and Molecular Bioengineering*, 5(2):227–238.

[He et al., 2016] He, C., Ni, X., Ge, H., Sun, X.-C., Chen, Y.-B., Lu, M.-H., Liu, X.-P., and Chen, Y.-F. (2016). Acoustic topological insulator and robust one-way sound transport. *Nature Physics*, 12(12):1124–1129.

[Hořava, 2005] Hořava, P. (2005). Stability of Fermi surfaces and K theory. *Physical Review Letters*, 95(1):016405.

[Hyman et al., 1992] Hyman, A., Middleton, K., and Centola, M. e. a. (1992). Microtubule-motor activity of a yeast centromere-binding protein complex. *Nature*, 359(533–536).

[J. Nettleton, 1993] J. Nettleton, J. H. e. a. F. G. B. (1993). Flexural rigidity of microtubules and actin filaments measured from thermal fluctuations in shape. *Journal of Cell Biology*, 120(4):923–934.

[Jiang et al., 2021] Jiang, B., Bouhon, A., Lin, Z.-K., Zhou, X., Hou, B., Li, F., Slager, R.-J., and Jiang, J.-H. (2021). Experimental observation of non-Abelian topological acoustic semimetals and their phase transitions. *Nature Physics*, pages 1–8.

[Jordan and Wilson, 2004] Jordan, M. A. and Wilson, L. (2004). Microtubules as a target for anticancer drugs. *Nature Reviews Cancer*, 4(253–265).

[Kaji et al., 2004] Kaji, N., Tezuka, Y., Takamura, Y., Ueda, M., Nishimoto, T., Nakanishi, H., Horiike, Y., and Baba, Y. (2004). Separation of long dna molecules by quartz nanopillar chips under a direct current electric field. *Analytical Chemistry*, 76(1):15–22.

[Kane, 2022] Kane, C. L. (2022). Quantized nonlinear conductance in ballistic metals. *Physical Review Letters*, 128:076801.

[Karoubi, 2008] Karoubi, M. (2008). *K-theory: An introduction*, volume 226. Springer Science and Business Media.

[Khanikaev et al., 2015] Khanikaev, A., Fleury, R., Mousavi, S., and Alù, A. (2015). Topologically robust sound propagation in an angular-momentum-biased graphene-like resonator lattice. *Nature Communications*, 6(8260).

[Kitaev, 2009] Kitaev, A. (2009). Periodic table for topological insulators and superconductors. *AIP Conference Proceedings*, 1134(1):22–30.

[Kruthoff et al., 2017] Kruthoff, J., de Boer, J., van Wezel, J., Kane, C. L., and Slager, R.-J. (2017). Topological classification of crystalline insulators through band structure combinatorics. *Physical Review X*, 7(4):041069.

[Kutchoukov et al., 2004] Kutchoukov, V., Laugere, F., van der Vlist, W., Pakula, L., Garini, Y., and Bossche, A. (2004). Fabrication of nanofluidic devices using glass-to-glass anodic bonding. *Sensors and Actuators A: Physical*, 114(2):521–527. Selected papers from Transducers 03.

[Lange et al., 1988] Lange, G., Mandelkow, E.-M., Jagla, A., and Mandelkow, E. (1988). Tubulin oligomers and microtubule oscillations. *European Journal of Biochemistry*, 178(1):61–69.

[Li et al., 2018] Li, F., Huang, X., Lu, J., Ma, J., and Liu, Z. (2018). Weyl points and Fermi arcs in a chiral phononic crystal. *Nature Physics*, 14(1):30–34.

[Liang et al., 2009] Liang, B., Yuan, B., and Cheng, J.-c. (2009). Acoustic diode: rectification of acoustic energy flux in one-dimensional systems. *Physical Review Letters*, 103(10):104301.

[Liu et al., 2021] Liu, C., Shi, J., Zhao, W., Zhou, X., Ma, C., Peng, R., Wang, M., Hang, Z. H., Liu, X., Christensen, J., Fang, N. X., and Lai, Y. (2021). Three-dimensional soundproof acoustic metacage. *Physical Review Letters*, 127:084301.

[Liu et al., 2014] Liu, Z. K., Zhou, B., Zhang, Y., Wang, Z. J., Weng, H. M., Prabhakaran, D., Mo, S.-K., Shen, Z. X., Fang, Z., Dai, X., Hussain, Z., and Chen, Y. L. (2014). Discovery of a three-dimensional topological Dirac semimetal, Na3Bi. *Science*, 343(6173):864–867.

[Loring, 2015] Loring, T. A. (2015). K-theory and pseudospectra for topological insulators. *Annals of Physics*, 356:383–416.

[Loring and Schulz-Baldes, 2017] Loring, T. A. and Schulz-Baldes, H. (2017). Finite volume calculation of K-theory invariants. *New York Journal of Mathematics*, 23:1111–1140.

[Loring and Schulz-Baldes, 2020] Loring, T. A. and Schulz-Baldes, H. (2020). The spectral localizer for even index pairings. *Journal of Noncommutative Geometry*, 14(1):1–23.

[Lu et al., 2016] Lu, J., Qiu, C., Ke, M., and Liu, Z. (2016). Valley vortex states in sonic crystals. *Physical Review Letters*, 116:093901.

[Lu et al., 2015] Lu, L., Wang, Z., Ye, D., Ran, L., Fu, L., Joannopoulos, J. D., and Soljačić, M. (2015). Experimental observation of Weyl points. *Science*, 349(6248):622–624.

[Lv et al., 2015] Lv, B. Q., Xu, N., Weng, H. M., Ma, J. Z., Richard, P., Huang, X. C., Zhao, L. X., Chen, G. F., Matt, C. E., Bisti, F., Strocov, V. N., Mesot, J., Fang, Z., Dai, X., Qian, T., Shi, M., and Ding, H. (2015). Observation of Weyl nodes in TaAs. *Nature Physics*, 11(9):724–727.

[Löwe et al., 2001] Löwe, J., Li, H., Downing, K., and Nogales, E. (2001). Refined structure of -tubulin at 3.5 Å resolution11edited by i. a. wilson. *Journal of Molecular Biology*, 313(5):1045–1057.

[M. F. Islam, 2010] M. F. Islam (2010). Normal modes and density of states of disordered colloidal solids. *Science*, 329(5992):656–658.

[Ma et al., 2019] Ma, G., Xiao, M., and Chan, C. (2019). Topological phases in acoustic and mechanical systems. *Nature Review Physics*, 1:281–294.

[Mahadevan and Mitchison, 2005] Mahadevan, L. and Mitchison, T. J. (2005). Cell biology: Powerful curves. *Nature*, 435:895–897.

[Martin et al., 1991] Martin, S. R., Schilstra, M. J., and Bayley, P. M. (1991). Opposite-end behaviour of dynamic microtubules. *Biochimica et biophysica acta*, 1073(3):555–561.

[Newton et al., 2002] Newton, C. N., Deluca, J. G., Himes, R. H., Miller, H. P., Jordan, M. A., and Wilson, L. (2002). Intrinsically slow dynamic instability of HeLa cell microtubules in vitro. *Journal of Biological Chemistry*, 277(45):42456–42462.

[Ni et al., 2019a] Ni, X., Chen, K., Weiner, M., Apigo, D. J., Prodan, C., Alù, A., Prodan, E., and Khanikaev, A. B. (2019a). Observation of hofstadter butterfly and topological edge states in reconfigurable quasi-periodic acoustic crystals. *Communications Physics*, 2(1):1–7.

[Ni et al., 2019b] Ni, X., Chen, K., Weiner, M., Apigo, D. J., Prodan, C., Alù, A., Prodan, E., and Khanikaev, A. B. (2019b). Observation of Hofstadter butterfly and topological edge states in reconfigurable quasi-periodic acoustic crystals. *Communications Physics*, 2(1):1–7.

[Ni et al., 2020] Ni, X., Li, M., Weiner, M., Alù, A., and Khanikaev, A. B. (2020). Demonstration of a quantized acoustic octupole topological insulator. *Nature Communications*, 11(1):2108.

[Ni et al., 2019c] Ni, X., Weiner, M., Alù, A., and Khanikaev, A. B. (2019c). Observation of higher-order topological acoustic states protected by generalized chiral symmetry. *Nature Material*, 18(2):113.

[Orr et al., 2003] Orr, G. A., Verdier-Pinard, P., McDaid, H., and Horwitz, S. B. (2003). Mechanisms of Taxol resistance related to microtubules. *Oncogene*, 22(47 REV. ISS. 6):7280–7295.

[Öz et al., 2019] Öz, R., Kk, S., and Westerlund, F. (2019). A nanofluidic device for real-time visualization of DNA-protein interactions on the single DNA molecule level. *Nanoscale*, 11(4):2071–2078.

[Ozawa et al., 2019a] Ozawa, T., Price, H. M., Amo, A., Goldman, N., Hafezi, M., Lu, L., Rechtsman, M. C., Schuster, D., Simon, J., Zilberberg, O., and Carusotto, I. (2019a). Topological photonics. *Reviews of Modern Physics*, 91:015006.

[Ozawa et al., 2019b] Ozawa, T., Price, H. M., Amo, A., Goldman, N., Hafezi, M., Lu, L., Rechtsman, M. C., Schuster, D., Simon, J., Zilberberg, O., and Carusotto, I. (2019b). Topological photonics. *Reviews of Modern Physics*, 91(1):015006.

[Peng et al., 2016] Peng, Y., Qin, C., and Zhao, D. e. a. (2016). Experimental demonstration of anomalous floquet topological insulator for sound. *Nature Communications*, 7(13368).

[Peri et al., 2020] Peri, V., Song, Z.-D., Serra-Garcia, M., Engeler, P., Queiroz, R., Huang, X., Deng, W., Liu, Z., Bernevig, B. A., and Huber, S. D. (2020). Experimental characterization of fragile topology in an acoustic metamaterial. *Science*, 367(6479):797–800.

[Po et al., 2017] Po, H. C., Vishwanath, A., and Watanabe, H. (2017). Symmetry-based indicators of band topology in the 230 space groups. *Nature Communications*, 8(1):50.

[Prodan et al., 2017] Prodan, E., Dobiszewski, K., Kanwal, A., Palmieri, J., and Prodan, C. (2017). Dynamical majorana edge modes in a broad class of topological mechanical systems. *Nature Communications*, 8(1):1–7.

[Prodan and Prodan, 2009] Prodan, E. and Prodan, C. (2009). Topological phonon modes and their role in dynamic instability of microtubules. *Physical Review Letters*, 103:248101.

[Qi et al., 2008] Qi, X.-L., Hughes, T. L., and Zhang, S.-C. (2008). Topological field theory of time-reversal invariant insulators. *Physical Review B*, 78:195424.

[Qi and Zhang, 2011a] Qi, X.-L. and Zhang, S.-C. (2011a). Topological insulators and superconductors. *Reviews of Modern Physics*, 83(4):1057.

[Qi and Zhang, 2011b] Qi, X.-L. and Zhang, S.-C. (2011b). Topological insulators and superconductors. *Reviews of Modern Physics*, 83(4):1057–1110.

[Qi et al., 2020] Qi, Y., Qiu, C., Xiao, M., He, H., Ke, M., and Liu, Z. (2020). Acoustic realization of quadrupole topological insulators. *Physical Review Letters*, 124:206601.

[Reisner et al., 2012] Reisner, W., Pedersen, J. N., and Austin, R. H. (2012). Dna confinement in nanochannels: physics and biological applications. *Reports on Progress in Physics*, 75(106601).

[Roll-Mecak, 2020] Roll-Mecak, A. (2020). The tubulin code in microtubule dynamics and information encoding. *Developmental Cell*, 54(1):7–20.

[Ryu et al., 2010] Ryu, S., Schnyder, A. P., Furusaki, A., and Ludwig, A. W. W. (2010). Topological insulators and superconductors: tenfold way and dimensional hierarchy. *New Journal of Physics*, 12(6):065010.

[Schnyder et al., 2008] Schnyder, A. P., Ryu, S., Furusaki, A., and Ludwig, A. W. W. (2008). Classification of topological insulators and superconductors in three spatial dimensions. *Physical Review B*, 78:195125.

[Schulz-Baldes and Stoiber, 2021] Schulz-Baldes, H. and Stoiber, T. (2021). Invariants of disordered semimetals via the spectral localizer. *Europhysics Letters*, 136:27001.

[Serra-Garcia et al., 2018] Serra-Garcia, M., Peri, V., Süsstrunk, R., Bilal, O. R., Larsen, T., Villanueva, L. G., and Huber, S. D. (2018). Observation of a phononic quadrupole topological insulator. *Nature*, 555(7696):342–345.

[Shi et al., 2009] Shi, J., Ahmed, D., Mao, X., Lin, S.-C. S., Lawit, A., and Huang, T. J. (2009). Acoustic tweezers: patterning cells and microparticles using standing surface acoustic waves (ssaw). *Lab on a Chip*, 9(20):2890–2895.

[Simon, 1978] Simon, B. (1978). Resonances and complex scaling: a rigorous overview. *International Journal of Quantum Chemistry*, 14(4):529–542.

[Singh et al., 2022] Singh, S., Prakash, O., and Bhattacharya, S. (2022). Hybrid fractal acoustic metamaterials for low-frequency sound absorber based on cross mixed micro-perforated panel mounted over the fractals structure cavity. *Scientific Report*, 12(20444).

[Song et al., 2016] Song, G. Y., Huang, B., Dong, H. Y., Cheng, Q., and Cui, T. J. (2016). Broadband focusing acoustic lens based on fractal metamaterials. *Scientific Report*, 6(35929).

[Su et al., 1979] Su, W., Schrieffer, J., and Heeger, A. J. (1979). Solitons in polyacetylene. *Physical Review Letters*, 42(25):1698.

[Sun et al., 2020] Sun, S., Song, Z., Weng, H., and Dai, X. (2020). Topological metals induced by the Zeeman effect. *Physical Review B*, 101(12):125118.

[Trout, 2000] Trout, J. (2000). On graded K-theory, elliptic operators and the functional calculus. *Illinois Journal of Mathematics*, 44(2):294–309.

[van den Heuvel et al., 2007] van den Heuvel, M. G. L., de Graaff, M. P., Lemay, S. G., and Dekker, C. (2007). Electrophoresis of individual microtubules in microchannels. *Proceedings of the National Academy of Sciences*, 104(19):7770–7775.

[Wang et al., 2005] Wang, Y. M., Tegenfeldt, J. O., Reisner, W., Riehn, R., Guan, X.-J., Guo, L., Golding, I., Cox, E. C., Sturm, J., and Austin, R. H. (2005). Single-molecule studies of repressor–dna interactions show long-range interactions. *Proceedings of the National Academy of Sciences*, 102(28):9796–9801.

[Wang et al., 2012] Wang, Z., Sun, Y., Chen, X.-Q., Franchini, C., Xu, G., Weng, H., Dai, X., and Fang, Z. (2012). Dirac semimetal and topological phase transitions in A_3Bi (A=Na, K, Rb). *Physical Review B*, 85(19):195320.

[Wang et al., 2013] Wang, Z., Weng, H., Wu, Q., Dai, X., and Fang, Z. (2013). Three-dimensional Dirac semimetal and quantum transport in Cd_3As_2. *Physical Review B*, 88(12):125427.

[Wen et al., 2019] Wen, X., Qiu, C., Qi, Y., Ye, L., Ke, M., Zhang, F., and Liu, Z. (2019). Acoustic Landau quantization and quantum-Hall-like edge states. *Nature Physics*, 15(4):352–356.

[Weng et al., 2015] Weng, H., Fang, C., Fang, Z., Bernevig, B. A., and Dai, X. (2015). Weyl semimetal phase in noncentrosymmetric transition-metal monophosphides. *Physical Review X*, 5(1):011029.

[Xia et al., 2008] Xia, Q., Morton, K. J., Austin, R. H., and Chou, S. Y. (2008). Sub-10 nm self-enclosed self-limited nanofluidic channel arrays. *Nano Letters*, 8(11):3830–3833.

[Xiao et al., 2015] Xiao, M., Chen, W.-J., He, W.-Y., and Chan, C. T. (2015). Synthetic gauge flux and Weyl points in acoustic systems. *Nature Physical*, 11(11):920–924.

[Xiao et al., 2017] Xiao, Y.-X., Ma, G., Zhang, Z.-Q., and Chan, C. T. (2017). Topological subspace-induced bound state in the continuum. *Physical Review Letters*, 118:166803.

[Xie et al., 2019] Xie, B., Liu, H., Cheng, H., Liu, Z., Chen, S., and Tian, J. (2019). Experimental realization of type-II Weyl points and Fermi arcs in phononic crystal. *Physical Review Letter*, 122(10):104302.

[Xu et al., 2015] Xu, Q., Song, Z., Nie, S., Weng, H., Fang, Z., and Dai, X. (2015). Two-dimensional oxide topological insulator with iron-pnictide superconductor lifeas structure. *Physical Review B*, 92(20):205310.

[Xu et al., 2020] Xu, Z.-x., Gao, H., Ding, Y.-j., Yang, J., Liang, B., and Cheng, J.-c. (2020). Topology-optimized omnidirectional broadband acoustic ventilation barrier. *Physical Review Applied*, 14:054016.

[Xue et al., 2021] Xue, H., Jia, D., Ge, Y., Guan, Y.-j., Wang, Q., Yuan, S.-q., Sun, H.-x., Chong, Y., and Zhang, B. (2021). Observation of dislocation-induced topological modes in a three-dimensional acoustic topological insulator. *Physical Review Letter*, 127(21):214301.

[Xue et al., 2019a] Xue, H., Yang, Y., Gao, F., Chong, Y., and Zhang, B. (2019a). Acoustic higher-order topological insulator on a kagome lattice. *Nature Material*, 18(2):108–112.

[Xue et al., 2019b] Xue, H., Yang, Y., Liu, G., Gao, F., Chong, Y., and Zhang, B. (2019b). Realization of an acoustic third-order topological insulator. *Physical Review Letter*, 122(24):244301.

[Yamamoto et al., 2009] Yamamoto, T., Maruyama, S., Nishiwaki, S., and Yoshimura, M. (2009). Topology design of multi-material soundproof structures including poroelastic media to minimize sound pressure levels. *Computer Methods in Applied Mechanics and Engineering*, 198(17):1439–1455.

[Yang et al., 2017] Yang, M., Chen, S., Fu, C., and Sheng, P. (2017). Optimal sound-absorbing structures. *Materials Horizons*, 4(4):673–680.

[Yang et al., 2019] Yang, Y., Sun, H.-x., Xia, J.-p., Xue, H., Gao, Z., Ge, Y., Jia, D., Yuan, S.-q., Chong, Y., and Zhang, B. (2019). Topological triply degenerate point with double Fermi arcs. *Nature Physical*, 15:645–649.

[Yang et al., 2015] Yang, Z., Gao, F., Shi, X., Lin, X., Gao, Z., Chong, Y., and Zhang, B. (2015). Topological acoustics. *Physical Review Letters*, 114(11):114301.

[Yeh et al., 2015] Yeh, J.-w., Sriram, K. K., Taloni, A., and Chen, Y.-l. (2015). Quantitative analysis of reptation of partially extended DNA in sub-30 nm nanoslits. *arXiv*, pages 1–24.

[Yokokawa et al., 2005] Yokokawa, R., Yoshida, Y., Takeuchi, S., Kon, T., and Fujita, H. (2005). Unidirectional transport of a bead on a single microtubule immobilized in a submicrometre channel. *Nanotechnology*, 17(1):289.

[Yuan and Fu, 2021] Yuan, N. F. Q. and Fu, L. (2021). Topological metals and finite-momentum superconductors. *Proceedings of the National Academy of Sciences*, 118(3):e2019063118.

[Zangeneh-Nejad and Fleury, 2020] Zangeneh-Nejad, F. and Fleury, R. (2020). Disorder-induced signal filtering with topological metamaterials. *Advanced Materials*, 32(28):2001034.

[Zhang et al., 2018a] Zhang, X., Xiao, M., Cheng, Y., Lu, M., and Christensen, J. (2018a). Topological sound. *Communications Physics*, 1.

[Zhang et al., 2018b] Zhang, Z., Tian, Y., Wang, Y., Gao, S., Cheng, Y., Liu, X., and Christensen, J. (2018b). Directional acoustic antennas based on valley-hall topological insulators. *Advanced Materials*, 30(36):1803229.

[Zhao et al., 2018] Zhao, X., Liu, G., Zhang, C., Xia, D., and Lu, Z. (2018). Fractal acoustic metamaterials for transformer noise reduction. *Applied Physics Letters*, 113(7).

[Zheng et al., 2022] Zheng, S., Man, X., Kong, Z.-L., Lin, Z.-K., Duan, G., Chen, N., Yu, D., Jiang, J.-H., and Xia, B. (2022). Observation of fractal higher-order topological states in acoustic metamaterials. *Science Bulletin*, 67(20):2069–2075.

[Zhu et al., 2011] Zhu, J., Christensen, J., Jung, J., Martin-Moreno, L., Yin, X., Fok, L., Zhang, X., and Garcia-Vidal, F. (2011). A holey-structured metamaterial for acoustic deep-subwavelength imaging. *Nature Physics*, 7(1):52–55.